The Thickness of High-Redshift Quasar Ionization Fronts as a Constraint on the Ionizing Spectral Energy Distribution

R. H. Kramer[1]* and Z. Haiman [1]*

[1] *Department of Astronomy, Columbia University, 550 West 120th Street, New York, NY 10027*

ABSTRACT

High–redshift quasars ($z \gtrsim 6$) drive ionization fronts into the intergalactic medium (IGM), with the thickness of the front generally increasing with the hardness of ionizing spectrum. If the thickness of the front can be measured, it can provide a novel constraint on the ionizing spectral energy distribution (SED), uniquely available for sources prior to the end of reionization. Here we follow the propagation of an I–front into a uniform IGM, and compute its thickness for a range of possible quasar spectra and ages, and IGM neutral hydrogen densities and clumping factors. We also explore the effects of uniform and non-uniform ionizing backgrounds. We find that even for hard spectra, the fronts are initially thin, with a thickness much smaller than the mean free path of ionizing photons. The front gradually thickens as it approaches equilibrium in $10^8 - 10^9$ years, and the thickness of its outer part can eventually significantly exceed simple estimates based on the mean free path. With a sufficiently high intrinsic hydrogen column density obscuring the source ($\log(N_{\rm H}/{\rm cm}^{-2}) \gtrsim 19.2$) or a sufficiently hard power–law spectrum combined with some obscuration (e.g. $d \log F_\nu / d \log \nu \gtrsim -1.2$ at $\log(N_{\rm H}/{\rm cm}^{-2}) \gtrsim 18.0$), the outer thickness of the front exceeds ~ 1 physical Mpc and may be measurable from the three–dimensional morphology of its redshifted 21cm signal. We find that the highly ionized inner part of the front, which may be probed by Lyman line absorption spectra, remains sharp for bright quasars unless a large obscuring column ($\log(N_{\rm H}/{\rm cm}^{-2}) \gtrsim 19.2$) removes most of their ionizing photons up to ≈ 40 eV. For obscured sources with $\log(N_{\rm H}/{\rm cm}^{-2}) \gtrsim 19.8$, embedded in a significantly neutral IGM, the black Lyman α trough (where the neutral fraction is $\sim 10^{-3}$) underestimates the size of the H II region by a factor of $\gtrsim 4$.

Key words: quasars:general – cosmology: theory – observation – diffuse radiation – radio lines: general – ultraviolet: general – quasars: absorption lines

1 INTRODUCTION

The spectra of $z > 6$ quasars (e.g. Fan et al. 2002; White et al. 2003), showing complete Gunn–Peterson (GP) absorption, have been widely analyzed as a possible probe of the ionization state of the ambient IGM. The sizes of inferred H II regions surrounding these sources depend on the neutral fraction (Cen & Haiman 2000; Madau & Rees 2000) and suggest a value above a few percent (Fan et al. 2002; Wyithe & Loeb 2004; Mesinger & Haiman 2004), although this inference is subject to some bias and significant scatter, depending on how the intrinsic H II region

size is deduced from the observed spectrum (Maselli et al. 2007; Bolton & Haehnelt 2007a,b). Direct evidence for a GP damping wing in the QSO spectra (Mesinger & Haiman 2004, 2007) also suggests that the neutral fraction exceeds several percent at least along two lines of sight. The evolution of Lyman α emitting galaxies may also suggest a significant global neutral fraction (Ota et al. 2007, although the presently observed evolution may still be attributed to the evolution in the halo abundance and in the mean IGM density; Dijkstra et al. 2007).

If the IGM is significantly neutral, then the shape of the I–front will be well–defined, i.e. the ionizing flux, over a region corresponding to the mean–free–path of ionizing photons, will be dominated by the quasar itself, rather than by the background. In this case, the shape of the I–front will

* E-mail: roban@astro.columbia.edu (RHK); zoltan@astro.columbia.edu (ZH)

contain information on the spectrum of the ionizing source. In particular, the thickness of the front is generally expected to increase for harder source spectra, whose typical ionizing photon has a longer mean free path (hereafter m.f.p.). Mesinger & Haiman (2004) noted that the onset of the Lyman α and β GP troughs in the spectra of $z > 6$ quasars occur at redshifts close to one another, corresponding to a physical separation of $R_\beta - R_\alpha \lesssim 1$ Mpc along the line of sight, possibly placing an upper limit on the hardness of the spectrum (with mean photon energy $\langle E \rangle < 230$ eV, for which the m.f.p. in a neutral IGM at $z \approx 6$ is ~ 1 Mpc). Although the ratio of oscillator strengths of the Lyman α and β lines is a factor of 5.2, once density inhomogeneities and foreground Lyman α absorption is taken into account, the Lyman β line effectively probes a factor of $2-3$ lower neutral fraction than Lyman α (Fan et al. 2002; Songaila & Cowie 2002). The comparison of R_β and R_α gives the path–length over which the neutral fraction rises by a factor of $2-3$; this could naively be taken as a proxy for the thickness of the I–front.

This simple interpretation, however, is complicated by possible absorption by the GP damping wing from the IGM (Mesinger & Haiman 2004, 2007), and also by the scatter in the R_β/R_α ratio expected to arise between different lines of sight due to density fluctuations (Bolton & Haehnelt 2007a). Nevertheless, if a sufficient number of distant quasars are detected in the future, the ratio R_β/R_α, and other features in their absorption spectra, could provide a diagnostic for a finite I–front thickness and therefore the hardness of the sources, at least statistically. Note that this test is not available at lower redshift, where the IGM is highly ionized, the m.f.p. of ionizing photons is already $\gtrsim 100$ Mpc, and photoionization equilibrium is established on a time–scale of $(\Gamma/n_H \lambda_{mfp})^{-1} \sim 10^4$ years, much less than the expected quasar lifetime.

Other methods have been proposed to probe the finite thickness of quasar I–fronts. Zaroubi & Silk (2005) explored measuring the thickness of I–fronts through their three–dimensional redshifted 21cm signatures, with a low-frequency radio telescope array such as LOFAR (for a comprehensive review of current and planned high-redshift 21-cm projects, see Furlanetto et al. 2006). The soft spectrum of stellar radiation would produce a much sharper ionization front than the very hard spectrum predicted to emerge from miniquasars; when the sources themselves are not detected, the 21cm maps could still discriminate between stellar– and quasar–driven reionization (Oh 2001). Finally, Cantalupo et al. (2007) recently suggested that collisionally excited Lyα emission may be detectable from the shell of material at the I–front, over an extended solid angle behind bright quasars; the spectral shape and thickness of this emission is another possible measure of the thickness of the I–front.

At present, little is known empirically about the ionizing spectrum of quasars at $z > 6$. At lower redshift, quasars are found to have relatively soft power-law spectra in the extreme ultraviolet, with an average spectral index of around $s = 1.8$ (Telfer et al. 2002). However, many quasars show a strong soft X–ray excess at a few 100eV, which can not be explained by thermal emission from a standard accretion disk. The excess X-rays could originate from Compton scattering in a hot corona surrounding the accretion disk

around the AGN (Porquet et al. 2004). Quasars at high redshift are also expected to be preferentially obscured due to the increased gas density, and may effectively radiate only at energies in soft X–rays bands and above (Sazonov et al. 2004). Shemmer et al. (2006) found that a composite X-ray spectrum of 21 $z > 4$ quasars had an effective spectral index in the X–ray of $s = 0.95$, and an intrinsic absorption column upper limit of $N_H \lesssim 6 \times 10^{22}$ cm^{-2}, consistent with the mean results from Just et al. (2007) at lower redshift.

Motivated by the suggestions above that the I–front thickness could be measurable, and by the lack of knowledge about the SEDs of high–z quasars, in this paper we follow the time–dependent propagation of an I–front into the IGM, and study its thickness for a range of possible spectra, quasar ages, clumping factors in the IGM, and various ionizing backgrounds. Our goal is to give a rough quantitative assessment of the conditions under which a hard spectrum may be diagnosed in future observations. Our modeling here extends the investigation of Zaroubi & Silk (2005), by exploring a range of quasar spectral parameters, by improving the treatment of helium and of secondary ionizations by energetic photoelectrons, and, most importantly, by following the time–dependent evolution of the non–equilibrium ionization structure. In an earlier study, Shapiro et al. (2004) used numerical simulations to study the evolution and properties of I–fronts propagating into the high–z IGM, for three different source spectra appropriate for massive population II and III stars and quasars. Our paper extends this work by including recombination radiation from helium, and by focusing on brighter sources and covering a larger range of spectra (including obscured spectra much harder than those examined by Shapiro et al.), for which the thickness may be directly measurable.

After we completed this paper, we became aware of the work of Thomas & Zaroubi (2007) who have recently made calculations similar to some of those presented here. We will compare our results further in § 6.

The rest of this paper is organized as follows. In § 2, we describe our modeling of the I–fronts, including treatments of the non–equilibrium evolution, and of helium. In § 3, we describe the salient features – evolution, shape and size – of the ionization front in our fiducial model for an obscured source with a hard spectrum. In § 4, we present our main results, discussing measurements of the thickness of the I–Front. In § 5, we reiterate the inherent limitations of our modeling approach, before finally, in § 6 we summarize our results and conclusions.

2   MODELING AND METHODS

In this section, we describe our model for computing the propagation of the I–front into a uniform medium. The modeling is rather standard for the most part, but we include a description of our own numerical implementation here for completeness, and in order to describe a few details about helium ionization that have typically not been included in previous works studying cosmological quasar H II regions.

2.1 Ionization and Recombination

Osterbrock & Ferland (2006) give an excellent description of one-dimensional spherical ionization structure calculations. For the most part we follow their methods, but we additionally include time evolution (non-equilibrium ionization states), secondary ionization by photoelectrons, and a full treatment of doubly-ionized helium.

We use the equations of one-dimensional radiative transfer to find the optical depth $\tau(\nu)$ as a function of distance from the quasar r and frequency ν. The optical depth contribution from each species is calculated at its ionization threshold:

$$\tau_{i,0}(r) = \int_0^r \sigma_{0,i}\, n_i(r')\, dr' \qquad (1)$$

where $n_i(r)$ is the number density of species i and $\sigma_{0,i}$ is the photoionization cross section at the threshold frequency $\nu_{0,i}$.[1] The optical depth contribution at any frequency is then $\tau_i(\nu) = \tau_{i,0}\, \sigma_i(\nu)/\sigma_{0,i}$ where $\sigma_i(\nu)$ is the cross section of species i at frequency ν. The total optical depth is the sum of contributions from all three species

$$\tau(\nu) = \tau_{\mathrm{HI}}(\nu) + \tau_{\mathrm{HeI}}(\nu) + \tau_{\mathrm{HeII}}(\nu) \qquad (2)$$

.

We ignore the effects of light travel time in calculating the ionization structure. As Cen & Haiman (2000) have pointed out, this ends up predicting the structure that is *observed* along the line of sight. Because of the finite speed of light, the evolution of the gas at a distance r from the quasar is retarded by the interval r/c. But an observer farther along the line of sight will also receive photons from that point earlier by an amount r/c. So in order to correctly predict the profile as it would be observed along the line of sight (for instance, in an absorption spectrum), we should add the two effects, which simply cancel each other out (White et al. 2003). If we wanted to predict the transverse structure as it would be observed, we could simply add in the appropriate delays after the evolution is calculated (Wyithe et al. 2005; Yu 2005; Shapiro et al. 2006).

For simplicity, we also ignore Hubble expansion. Even at $z = 6$, a quasar lifetime of 10^8 years is much shorter than the Hubble time. We do note, however, that the changing density of the IGM could make a discernible difference to the shape of the ionization profile, especially for the largest or thickest H II regions, which extend to several percent of the Hubble radius.

The photoionization rate of species i (per atom) is

$$\Gamma_i = \int_{\nu_{0,i}}^{\infty} d\nu\, \frac{L_\nu}{h\nu}\, \sigma_i(\nu)\, \frac{e^{-\tau(\nu,r)}}{4\pi r^2} \qquad (3)$$

where L_ν is the specific luminosity, and r is the distance from the source. In our numerical ionization code, we tabulate Γ_i as a function of $\tau_{\mathrm{HI},0}$, $\tau_{\mathrm{HeI},0}$, and $\tau_{\mathrm{HeII},0}$ before calculating the evolution of the ionization structure. Added to that rate for hydrogen is a position-independent background

photoionization rate, parametrized by the resulting equilibrium ionized fraction $X_{\mathrm{HII},BG}$:

$$\Gamma_{BG} = C\alpha_B n_{\mathrm{H}}\, \frac{X_{\mathrm{HII},BG}^2}{1 - X_{\mathrm{HII},BG}} \qquad (4)$$

where α_B is the so-called "case B" recombination rate (the recombination coefficient to all excited levels of hydrogen, evaluated at $T_{\mathrm{gas}} = 10^4$ K unless otherwise specified) and C is the clumping factor $C \equiv \langle n_{\mathrm{H}}^2 \rangle / \langle n_{\mathrm{H}} \rangle^2$. This background arises from preexisting galaxies, and is expected to consist of a patchwork of H II bubbles surrounded by a relatively neutral IGM. Note that even if the ionization outside the quasar's H II region is patchy (with a swiss–cheese topology), as it is expected to be, in the interior of the H II region, where the low neutral fraction results in a long m.f.p., it will be much more uniform (and will also have a higher amplitude). There will, however, be a radial profile to the background flux, due to the clustering of galaxies around the quasar (Wyithe & Loeb 2007; Lidz et al. 2007; Alvarez & Abel 2007). We will first ignore these effects, assuming that the I–front is located sufficiently far away that this bias is small, and that we are averaging the I-front over many small galaxy–bubbles. However, in § 4.2.4, we will return to this issue, where we will also explore various models for a non–uniform ionizing background.

In addition to the quasar's radiation and the UV background, several other processes occur in the gas that affect the ionization balance and couple the ionization states of hydrogen and helium.

Photoelectrons produced during ionization carry residual energy that can cause further ionizations (Shull & van Steenberg 1985). In our calculations we include the secondary ionization of hydrogen by photoelectrons from both hydrogen and helium, and treat it as an on-the-spot process (the latter assumption is justified similarly to the argument for case-B recombination, since the collisional ionization cross–section is typically larger than the photo–ionization cross–section; Shull & van Steenberg 1985). We use the fitting formula provided by Dijkstra et al. (2004) in the high-energy limit to calculate the fraction of energy $\phi(X_e)$ each photoelectron will expend in further ionizations of hydrogen. Using the high-energy limit introduces only a small error since low-energy photons cause few secondary ionizations in any case and the function quickly approaches its asymptotic value as the photon energy increases. Note that in the original calculations of $\phi(x)$, Shull & van Steenberg (1985) defined $x \equiv n_{\mathrm{HII}}/n_{\mathrm{H}}$ and assumed $n_{\mathrm{He}}/n_{\mathrm{H}} = 0.1$ (versus 0.079 in our model), and $X_{\mathrm{HeII}} = X_{\mathrm{HII}}$ (where $X_{\mathrm{HeII}} \equiv n_{\mathrm{HeII}}/n_{\mathrm{He}}$). While neither of those conditions holds exactly in our models, they are reasonable approximations. To account approximately for the extra electrons introduced by doubly-ionized helium (which was not included originally) we use $x = X_{\mathrm{HII}} + (n_{\mathrm{He}}/n_{\mathrm{H}})X_{\mathrm{HeIII}}$ (where $X_{\mathrm{HeIII}} \equiv n_{\mathrm{HeIII}}/n_{\mathrm{He}}$). It is a small effect in any case, since HeIII is formed only where hydrogen is already highly ionized, and ϕ vanishes as x approaches unity.

We neglect secondary ionizations of helium which happen at less than 20% of the rate of hydrogen. The mean number of secondary ionizations of hydrogen per photoelectron produced in the ionization of species i is

---

[1] Threshold ionization cross sections were taken from Osterbrock & Ferland (2006) for H I and He II and from Hummer & Storey (1998) for He I. At other frequencies, we used the fitting formulae from Yan et al. (1998) for He I and from Osterbrock & Ferland (2006) for H-like ions.

$$n_2 = \phi(X_e)\, \frac{\langle E_i \rangle - h\nu_{0,i}}{h\nu_{0,\mathrm{HI}}} \tag{5}$$

where $\langle E_i \rangle$ is the mean energy of photons locally ionizing species i:

$$\langle E_i \rangle = \frac{1}{\Gamma_i} \int_{\nu_{0,i}}^{\infty} d\nu\, (h\nu)\, \sigma_i(\nu)\, \frac{L_\nu}{h\nu}\, \frac{e^{-\tau(\nu,r)}}{4\pi r^2} \tag{6}$$

Similarly to Γ_i, we tabulate $\langle E_i \rangle$ as a function of $\tau_{\mathrm{HI},0}$, $\tau_{\mathrm{HeI},0}$, and $\tau_{\mathrm{HeII},0}$, before integrating the ionization structure.

Photons produced during recombination of hydrogen and helium are also included in our code in the on-the-spot approximation. High-frequency recombination radiation is capable of ionizing neutral hydrogen and helium, as well as singly-ionized helium, so the fraction of recombination photons ultimately ionizing each species must be calculated. In general the fraction of photons of frequency ν that ionize species i is

$$y_i(\nu) = \frac{\sigma_i(\nu)\, n_i}{\sigma_{\mathrm{HI}}(\nu)\, n_{\mathrm{HI}} + \sigma_{\mathrm{HeI}}(\nu)\, n_{\mathrm{HeI}} + \sigma_{\mathrm{HeII}}(\nu)\, n_{\mathrm{HeII}}} \tag{7}$$

The overall fraction for a given recombination process is an average of $y_i(\nu)$ over the spectrum of the emitted radiation. In our calculations, we make the simplifying assumptions that all H I, He I and He II Lyman continua, and He II Balmer continuum photons are produced with the minimum energy. The first and last of these occur below the threshold for all species but HI. The He II Lyman α line is treated similarly, assuming all photons have the mean energy of that line.

Certain higher He I lines produces in the recombination cascade are energetic enough to ionize hydrogen, with an average of 0.96 H-ionizing photons ultimately produced for each recombination to any excited level of HeI (in the low-density limit which applies here, Osterbrock & Ferland 2006). Another source of ionizing photons is the transition from the first excited level to the ground state of HeII: instead of producing a He II Lyman α photon, it can instead occur via a two-photon process. We calculate the fraction of recombinations to all excited states of HeII that end in a two-photon emission (as a function of temperature) by interpolating the tabulated values from Hummer & Seaton (1964). An average of 1.425 photons capable of ionizing hydrogen and 0.737 capable of ionizing neutral helium are produced for each two-photon event (Flower & Perinotto 1980), the latter of which are assumed to have the threshold ionization energy for helium.

We use recombination rate coefficients from Hui & Gnedin (1997), except for the coefficient for recombinations directly to the $n = 2$ level of HeII, which is taken from Ferguson & Ferland (1997). All calculations presented in this paper assume an isothermal gas of constant mean density and clumping factor.

2.2 The Ionization Structure

The ionization structure surrounding the quasar is calculated by integrating the net ionization rates over time. Before the first iteration, an array of $(X_{\mathrm{HII}}, X_{\mathrm{HeII}}, X_{\mathrm{HeIII}})$ values, corresponding to a sequence of r values, is initialized to $(X_{\mathrm{HII},BG}, 0, 0)$. The ionization and recombination rates are calculated as described above and used to find dX_{HII}/dt,

dX_{HeII}/dt, and dX_{HeIII}/dt. The integration time step is calculated using

$$\Delta t = \frac{F_{dt}}{\max(\Gamma_{\mathrm{HI}} X_{\mathrm{HI}},\; \Gamma_{\mathrm{HeI}} X_{\mathrm{HeI}},\; \Gamma_{\mathrm{HeII}} X_{\mathrm{HeII}})} \tag{8}$$

where $F_{dt} = 0.004$ is just a numerical parameter optimized by trial and error. Decreasing F_{dt} by a factor of two (improving the time resolution) has no important effect on the results. The time step is only updated every 10 iterations, and to help damp numerical oscillations we actually use $\Delta t_{\mathrm{new}} = 0.75\,\Delta t_{\mathrm{old}} + 0.25\,\Delta t$ as the time step.

In order to increase the speed and stability of the integration, the ionized fractions for the inner part of the array (at low r) are frozen and no longer recalculated once a stable equilibrium is achieved. Every tenth iteration we calculate the maximum radius at which the ionization states are in equilibrium, defined as $r_{\mathrm{eq}} = \max(r)$ for which

$$X_{\mathrm{HI}} \left(\frac{dX_{\mathrm{HII}}}{dt} \right)^{-1} > 5 \times 10^7\, \Delta t \tag{9}$$

$$X_{\mathrm{HeII}} \left(\frac{dX_{\mathrm{HeIII}}}{dt} \right)^{-1} > 5 \times 10^7\, \Delta t \tag{10}$$

$$\tau_{\mathrm{HI},0} < 1000 \tag{11}$$

The last condition on the optical depth is introduced to exclude regions far ahead of the front, where time scales grow long because the radiation field is so weak. For runs with a high uniform ionizing background we decreased the optical depth limit to $\tau_{\mathrm{HI},0} < 100$ because of the reduced opacity. Once r_{eq} is found, the next iteration is begun, and the ionized fractions at $r > r_{\mathrm{eq}}$ are updated (and constrained to the interval $[0,1]$). Using our fiducial parameters (described below and in § 3), it took 76000 iterations to evolve the structure through 5×10^8 years.

2.3 Numerical Parameters

As mentioned above, ionization rates and mean photon energies are tabulated as a function of the threshold optical depths of each species. The quantities are evaluated on a grid of logarithmically spaced values of $\tau_{\mathrm{HI},0}$, $\tau_{\mathrm{HeI},0}$, and $\tau_{\mathrm{HeII},0}$. The dimensions of the ionization rate grids are 332 by 301 by 301 values, while the mean photon energy grids are 416 by 61 by 61 values. Each optical depth range extends from 10^{-8} up to the maximum optical depth for which $\Gamma_i/\max(\Gamma_i) > 10^{-6}$, which depends on the source spectrum.

The simulations presented here use a grid of 1300 equally spaced radius values, extending from 5×10^4 pc (all distances in this paper are in proper, not comoving, units unless stated otherwise) to $1.5\, R_{\mathrm{Strom}}$, where R_{Strom} is the radius of the classic equilibrium Strömgren sphere,

$$R_{\mathrm{Strom}} \equiv \left(\frac{Q}{\frac{4}{3}\pi n_{\mathrm{H}}^2 \alpha_B C} \right)^{\frac{1}{3}}. \tag{12}$$

Note that this expression ignores helium and secondary ionizations. With $Q = 2 \times 10^{57}\ s^{-1}$ and $C = 1$, $R_{\mathrm{Strom}} = 22.2$ Mpc at $z = 6$.

We tested for convergence by doubling the resolution, which had no effect on the results. For our canonical parameters the step size works out to $\Delta r = 2.56 \times 10^{-2}$ Mpc with an outer radius of 33.4 Mpc.

We have tested our code several ways to ensure reasonable numerical performance. As mentioned above, we tested for convergence by doubling either the time or spatial resolution, neither or which had any important effect on the results. Using a soft spectrum (so that the front is sharp) we find very good agreement with analytical estimates for ionized region size and front velocity. We also find agreement with the Cosmological Radiative Transfer Codes Comparison Project ("test 1" in Iliev et al. 2006) calculations, and the examples presented in Osterbrock & Ferland (2006).

2.4 Physical Parameters

The temperature of the gas is important, because it controls the recombination rates. All calculations presented in this paper assume an isothermal gas. We justify this assumption by noting that most of the photoionization heating occurs somewhat ahead of the front where the ionized fractions are small and recombination rates are therefore low, whereas the temperature inside the front is fairly uniform (as can be seen in Bolton & Haehnelt 2007b; Iliev et al. 2006). We experimented with introducing artificially varying temperature profiles in the outer regions of the front. We made the temperature a function of optical depth so that the temperature variations would be tied to the location of the front. We tried several profiles, from smooth functions mimicking the temperature profiles in the appendix of Bolton & Haehnelt (2007b), to a step function increasing the temperature by a factor of 5 beyond $\tau_{\mathrm{HI},0} \geq 0.001$. We found that none of these had a significant effect on the profile, as long as the variation occurred outside of the region that had reached equilibrium. The ionization rate totally dominates the recombination rate in the moving part of the front, reaching parity only as the ionized fraction approaches equilibrium. We conclude that since the heating of the gas occurs before it reaches ionization equilibrium, and since the exact recombination rate is irrelevant outside of the equilibrium region, changes in the recombination rate due to temperature variations will not be an important factor in determining the shapes of the fronts.[2]

We assume the number density of hydrogen atoms surrounding our sources is the mean density of the IGM at $z = 6$, $n_{\mathrm{H}} = 2.2 \times 10^{-7}\,\mathrm{cm}^{-3}(1+z)^3 = 7.6 \times 10^{-5}\,\mathrm{cm}^{-3}$. The helium mass fraction is 0.24, yielding $n_{\mathrm{He}} = 6.0 \times 10^{-6}\,\mathrm{cm}^{-3}$. The electron temperature is $T_{\mathrm{gas}} = 10^4$ K. For our fiducial case we use a clumping factor of $C = 1$.

The spectra we have used are absorbed power laws, as show in Figure 1, with specific luminosity

$$L_\nu \propto \nu^{-s} \exp\left(-N_{\mathrm{H}}\left[\sigma_{\mathrm{HI}}(\nu) + \frac{n_{\mathrm{He}}}{n_{\mathrm{H}}}\sigma_{\mathrm{HeI}}(\nu)\right]\right),\quad(13)$$

where s is the spectral index and N_{H} and N_{He} are the column densities of hydrogen and helium intrinsic to the source. The spectrum is normalized to produce ionizing photons at rate Q before the absorption, so the ionizing photon luminosity after absorption Q_{abs} can be much lower. Note that high

[2] Changes in temperature due to radiative transfer can also have dynamical effects on the gas around the I-front; but in the limit where the recombination rate is unimportant, our conclusions on the ionized fraction should also be insensitive to such dynamical effects.
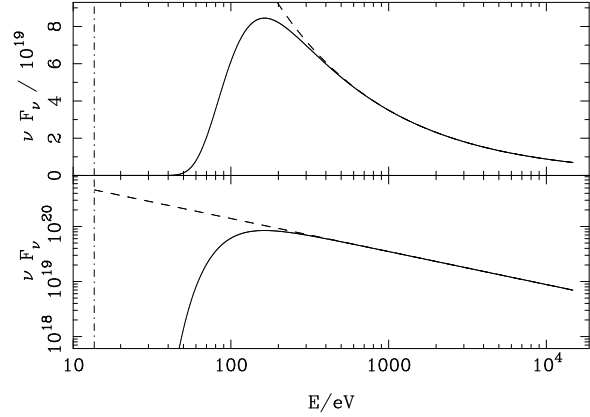
Figure 1. An absorbed power law spectrum (arbitrary units) with $s = 1.6$ and $N_{\mathrm{H}} = 10^{19.2}$ cm^{-2} (solid curves) plotted in linear (upper panel) and logarithmic (lower panel) flux units. The dashed lines show the unabsorbed spectrum. The vertical dot-dashes lines indicate the hydrogen ionization threshold at 13.6eV.

energy photons can cause multiple secondary ionizations, so Q_{abs} is not exactly the total ionization rate the spectrum produces. It is difficult to take secondary ionizations into account *a priori*, since (as we discussed earlier) the number of secondary ionizations is a strong function of the local free electron density, and therefore depends on where the photon is absorbed. Other factors can have an even larger effect on the ionizing efficiency of the spectrum, such as the fact that the hardest photons can escape the region entirely.

As mentioned in the Introduction, the ionizing spectra of quasars at $z > 6$ is uncertain. For our fiducial model for an obscured source, we have chosen $Q = 2 \times 10^{57}\,\mathrm{s}^{-1}$ (corresponding roughly to the expected value for the $z \sim 6$ quasars in the SDSS; e.g. Mesinger & Haiman 2004), $s = 1.6$, and $\log(N_{\mathrm{H}}/\mathrm{cm}^{-2}) = 19.2$ (which results in a post-absorption photon luminosity of $Q_{\mathrm{abs}} = 8.3 \times 10^{55}\,\mathrm{s}^{-1}$). We will consider variations in the power–law index and obscuring column density that are consistent with expectations based on the lower redshift data.

3 EVOLUTION, SHAPE AND SIZE OF THE IONIZATION FRONT

In this section, we present our results for the time–evolving I–front around a fiducial source with hard spectrum, and discuss the broad features that can be relevant to future measurements. Quantitative results will be presented and discussed in the next section.

3.1 The Time-Evolving Ionization Front

An often used proxy for the thickness of an ionization front around a quasar is the mean free path $l_{\mathrm{MFP}} = [\,n_{\mathrm{HI}}\,\sigma_{\mathrm{HI}}(\langle\nu\rangle)\,]^{-1}$, where $\langle\nu\rangle$ is a characteristic frequency of the ionizing photons. The thickness can be estimated, for example, by adopting $n_{\mathrm{HI}} = 0.5\,n_{\mathrm{H}}$, and the mean frequency of ionizing photons emitted by the quasar for $\langle\nu\rangle$. The resulting value of l_{MFP}, however, is an accurate proxy for the thickness of the I–front only for particular definitions of the thickness, and only under particular conditions. For

instance, the ionizing spectrum is hardened as the photons travel outward through the gas, since low-energy photons are more readily absorbed. As a result, the outer edge of the front will be spread over a longer path than the inner edge.

Another complication is that the ionization fronts around short–lived quasars are expected to be propagating outward (rather than corresponding to the static edge of an equilibrium Strömgen sphere), which has a strong effect on the shape of the front. It is widely noted (e.g., Shapiro & Giroux 1987) that the ionization state of the gas surrounding a typical high-redshift quasar will not have time to reach equilibrium with the radiation field during a quasar lifetime of 10^7 to 10^8 years,[3] since the time scale to reach equilibrium is roughly the recombination time $t_{\rm rec} = (C\,\alpha_B\,n_{\rm H})^{-1} = 1.62 \times 10^9\,C^{-1}\,[(1+z)/7]^{-3}$ years. This timescale can also be thought of as the time required for the source to emit one photon for each hydrogen atom within the Strömgren sphere. Throughout the process of establishing equilibrium, the shape of the ionization front is changing, therefore we must take into account non-equilibrium effects in order to correctly predict the ionization front thickness.

Figure 2 shows the evolution of the ionization structure around our fiducial absorbed power–law source. The hydrogen front starts out quite thin, but becomes thicker and thicker as it propagates outward. When the source is turned on, the gas closest to it is very quickly ionized up to its equilibrium level, while gas a little further away is ionized much more slowly, due both to the intervening absorption and geometric dilution of the radiation. This means that the inner edge of the front is evolving faster than the outer edge, which effectively tilts the $X_{\rm HI}$ curve, making it steeper. This creates a very thin transition region at first, which thickens as the front propagates outward and slows down. Depending on how the thickness of the front is measured, it can start out thinner than the mean free path, and end up much thicker.

These effects can be seen even with a monochromatic spectrum, but, as illustrated in Figure 3, a spectrum with a broad continuum of ionizing radiation can enhance the effect. Early on (e.g. at 10^6 years), photons with lower energy (and therefore high ionization cross section) will dominate the ionization at the front, while higher-energy photons escape to larger distances and pre-ionize the medium (as seen in the long tail of curves representing the ionized fraction). This makes the front relatively thin because of the short mean free path of these photons. As the front moves outward (e.g at 10^8 years), the lowest energy photons will continue to be preferentially absorbed closer to the source (and will dominate the ionization balance in the inner regions), leaving the higher-energy photons to dominate in the outer parts of front. This hardened spectrum creates a thicker front because of the longer mean free path.

Based on the above features, it will be useful for the discussion below to divide a snapshot of the ionization structure at a time $t < t_{\rm rec}$ into three distinct regions: Closest to the quasar, in the *equilibrium zone*, the ionization rate has al-

---

[3] A combination of overdensity and high clumping factors in the typical quasar environment could, however, reduce the recombination time to a value perhaps as short as $\sim 5 \times 10^6$ years at $z = 6.4$ (Yu & Lu 2005).
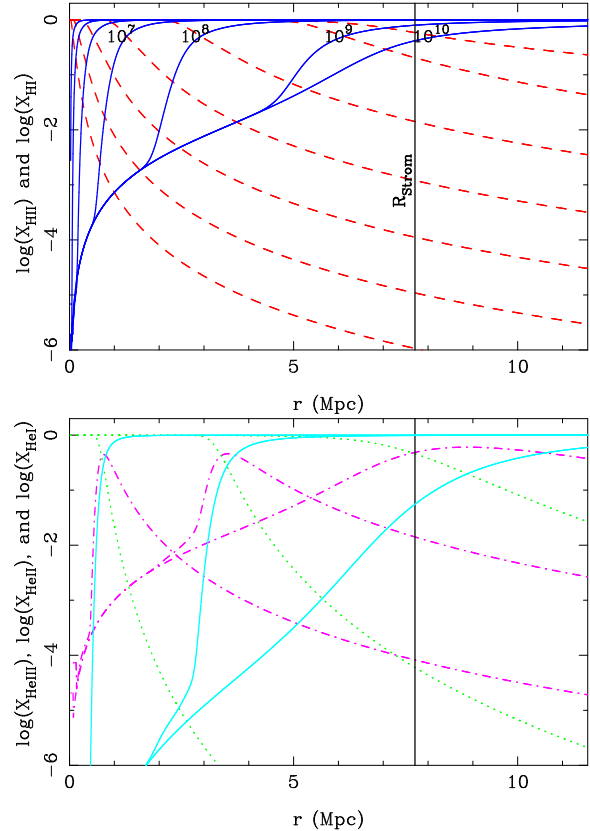

Figure 2. Ionized (dashed red) and neutral (solid blue) hydrogen fractions (a); and neutral (solid cyan), singly-ionized (dot-dashed magenta) and doubly-ionized (dotted yellow) helium fractions (b) versus radius (proper coordinates). Curves in the upper are for quasar ages of $4 \le \log(t/{\rm years}) \le 10$ in 1 dex increments. In the lower panel, only $\log(t/{\rm years}) = 6, 8$, and 10 are shown for clarity. By 10^{10} years the entire ionization structure is in equilibrium. Model parameters are $Q = 2 \times 10^{57}\,{\rm s}^{-1}$; $s = 1.6$; $\log(N_{\rm H}/{\rm cm}^{-2}) = 19.2$. The mean photon energy for this spectrum is ≈ 240 eV, and the corresponding mean free path is ~ 3 (proper) Mpc.

ready reached equilibrium with the recombination rate. Just outside the equilibrium region is a *rapid–ionization zone*, where relatively neutral gas is suddenly being exposed to intense ionizing radiation. Further out there is a *pre–ionization zone*, where the relatively rare high-energy photons penetrate and begin to ionize the gas, but recombination rates are low because of the low ionized fraction.

Figure 4 shows a snapshot of the local mean ionizing photon energy (equation 6), and the corresponding mean free path (calculated using the local neutral fraction), versus neutral hydrogen fraction, for the profile at 10^8 years shown in Figure 2. The spectrum is relatively unaffected by hardening up to $X_{\rm HI} \approx 0.1$, but the mean energy increases rapidly after the neutral fraction reaches 0.3. Similarly, the mean free path at first decreases in inverse proportion to the increasing neutral fraction, but reaches a minimum at $X_{\rm HI} \approx 0.3$ and begins to grow as the spectrum hardens. This explains why the outer tail of ionization is so thick compared to the inner face of the front. If we measure the thickness of the front from $X_{\rm HI} = 0.1$ to 0.9, we find (as shown in the figure) that it is barely consistent with the range of $l_{\rm MFP}$ over the same interval: both approaches to estimating the $l_{\rm MFP}$
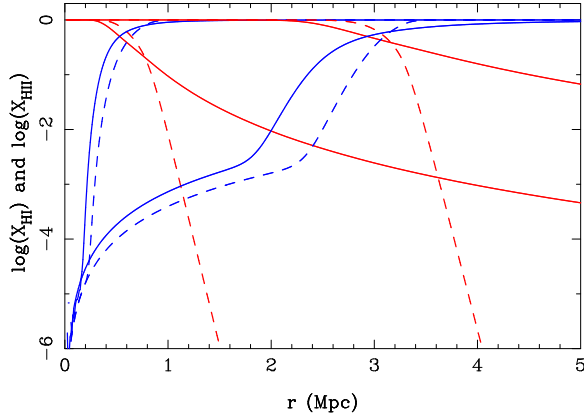
Figure 3. Ionization structure for an absorbed power law spectrum (solid, same parameters as Figure 2) and for a monochromatic spectrum (dashed). Ionized (red, decreases with r) and neutral (blue, increases with r) hydrogen fractions are shown at $t = 10^6$ years (left set of curves) and $t = 10^8$ years (right set of curves). The monochromatic spectrum is normalized to produce ionizing photons at the same rate $Q_{\rm abs} = 8.3 \times 10^{55}$ s^{-1} and has a photon energy of 89 eV, which is the local mean ionizing photon energy (weighted by cross section) $\langle E_{\rm H} \rangle$ of the absorbed power law spectrum. Note that a convenient way to estimate the thickness of the front is to compare where the ionized and neutral fraction curves cross $\log(X) \approx -1$ at a given time.
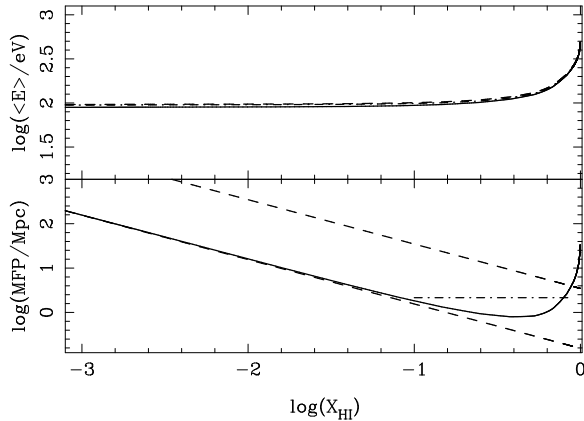

Figure 4. The upper panel shows the mean ionizing photon energy $\langle E_{\rm H} \rangle$ for hydrogen (solid curve), neutral helium (dashed curve), and singly-ionized helium (dot-dashed curve). The lower panel shows the local mean free path versus neutral hydrogen fraction at 10^8 years (solid curve; using the same model as in Figure 2). The lower dashed line shows $l_{\rm MFP}$ calculated using the $\tau = 0$ value for the local mean ionizing photon energy (weighted by cross section) $\langle E_{\rm H} \rangle = 89$ eV, while the upper dashed line is calculated using the $\tau = 0$ overall mean ionizing photon energy $\langle E \rangle = 239$ eV. The horizontal dot-dashed line indicates the thickness of the front as measured from $X_{\rm HI} = 0.1$ to 0.9.

based on an average photon energy of the source become inaccurate because of the spectral hardening. The intersection of the three curves at $\log(X_{\rm HI}) = -0.1$ is merely a coincidence. Indeed, recall that the ionization structure is not in equilibrium, so the width is constantly changing. The estimate of the m.f.p. based on the mean photon energy of 239 eV and a neutral medium yields ~ 3 Mpc, whereas the path corresponding to the range $0.1 < X_{\rm HI} < 0.9$ in the equilibrium case is much longer, ~ 15 Mpc.
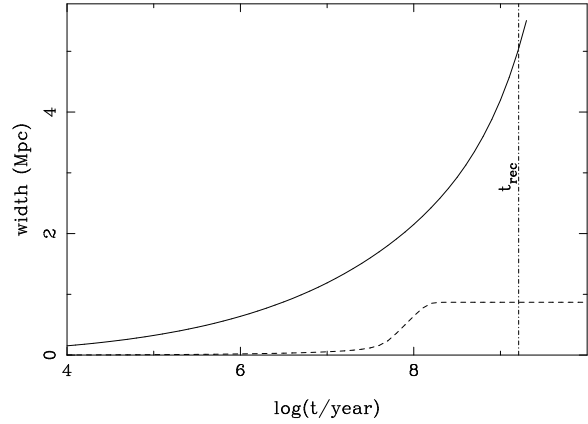
Figure 5. Width measurements versus time for the ionization front shown in Figure 2. The solid curve shows the thickness of the front as measured from $X_{\rm HI} = 0.1$ to 0.9, while the dashed curve shows the thickness between $X_{\rm HI} = 10^{-3}$ and $10^{-2.5}$.
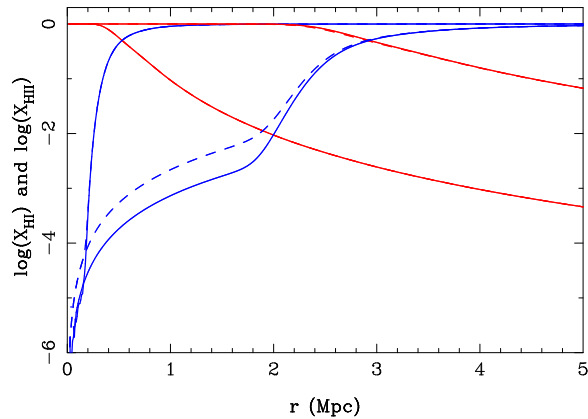

Figure 6. Ionization structure with (solid) and without (dashed) ionization of hydrogen by helium recombination photons. Ionized (red, decreases with r) and neutral (blue, increases with r) hydrogen fractions are shown at $t = 10^6$ years (left set of curves) and $t = 10^8$ years (right set of curves). Note that this recombination radiation accounts for almost all of the influence of helium on the hydrogen ionization structure.

Figure 5 shows two different measurements of the thickness of the front versus the logarithm of the time. The definitions of these thicknesses will be justified in § 4, but for now we note that the outer part of the front grows thicker all the way up to about $t_{\rm rec}$, while the inner part of the front comes into equilibrium much sooner.

The presence of helium also has important effects on the hydrogen ionization structure, as can be seen in Figure 6. The influence is due to the coupling of the ionization states by recombination radiation. By reprocessing high-energy photons (which, in the absence of helium, would escape to large distances) into lower-energy recombination radiation (which is absorbed on the spot, mostly by hydrogen), helium lowers the hydrogen neutral fraction in the equilibrium zone. The difference is a factor of ~ 3 in the region where $X_{\rm HI} \lesssim 10^{-2}$ at 10^8 years; this region is relevant in the analysis of the proximity zone of the quasar in Lyα/β absorption. In particular, neglecting helium can result in predicting a much thicker front, depending on how thickness is
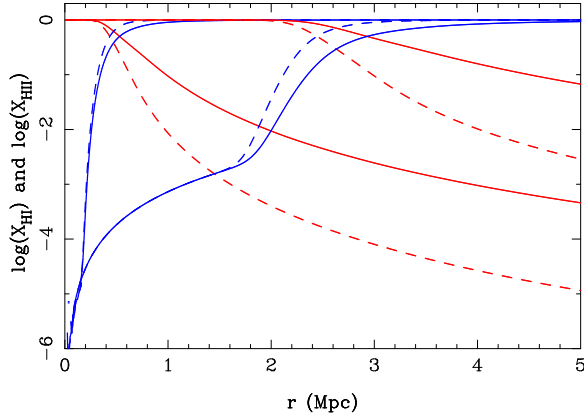
Figure 7. Ionization structure with (solid) and without (dashed) secondary ionizations by high energy photoelectrons. Ionized (red, decreases with r) and neutral (blue, increases with r) hydrogen fractions are shown at $t = 10^6$ years (left set of curves) and $t = 10^8$ years (right set of curves).

Figure 8. Ionized and neutral hydrogen fractions for a source with no intrinsic absorption ($N_H = 0$, dashed) or with $\log(N_H/\text{cm}^{-2}) = 19.2$ (solid). Spectra are normalized to produce the same number of photons $Q_{\text{abs}} = 8.3 \times 10^{55}$ s^{-1}. Other spectral parameters are the same as in Figure 2.

measured (and a factor of several too large R_β/R_α ratio; see below).

Secondary ionizations have a similarly important effect, but on the outer tail of the ionization structure, as shown in Figure 7. Neglecting secondary ionizations can reduce the thicknesses we would predict in the outer part of the front by several Mpc.

3.2 The Effects of Spectral Hardness

As evident from the above discussion, the shape and hardness of the spectrum can have dramatic effects on the ionization structure. Generally a harder spectrum will produce thicker fronts, although as we shall see below, this is not always the case for certain definitions of front thickness. The mean photon energy is not enough to characterize the shape of the ionization structure it will produce. For instance, even a relatively weak high-energy component can produce an enhanced pre-ionization region, while a low-energy component can increase the ionized fraction of the equilibrium region but have little effect on the thickness of the rapid–ionization zone. Enhancing the effect of a high-frequency component is the fact that energetic photons can cause multiple secondary ionizations, especially in a relatively neutral medium.

A harder spectrum will also generally produce a "shallower" ionized region, in the sense that the ionized fraction will be lower in the inner part of the ionized region since the ionization cross section is lower for high-energy photons. At the quasar ages we are considering this effect can be considered to affect mainly the equilibrium region.

Two parameters control the shape of the spectrum in our models. Increasing the spectral index s makes the spectrum softer, while increasing the intrinsic hydrogen column density N_H cuts off more low-energy emission, hardening the spectrum.

For reference, Figure 8 shows the fronts produced by a spectrum with no intrinsic absorption ($N_H = 0$). As expected, the fronts are much sharper than those in Figure 2.
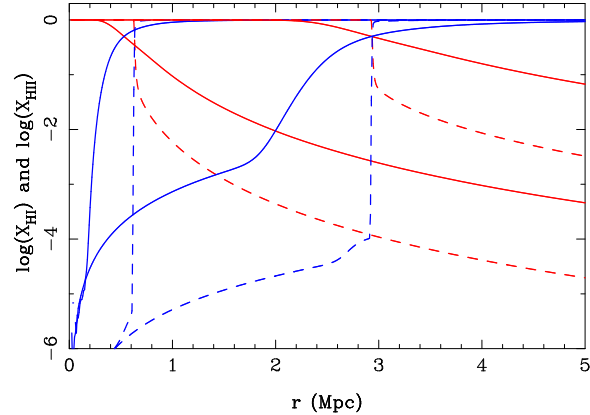
3.3 The Size of the Ionized Region

Before discussing the thickness of the I–fronts in detail in the next section, it is useful to discuss the overall size of the H II region. As mentioned in the Introduction, the size of the H II regions could be probed either in 21cm studies, or by Lyman line absorption spectra of individual sources. The former technique is sensitive to $X_{HI} \sim 1$, whereas the latter technique (with typical deep Keck spectra) probes the much lower neutral fraction $X_{HI} \sim 10^{-3}$. In Figure 9, we therefore show the size of the ionized region measured out to $r_{0.5}$, where $X_{HI} = 0.5$ (top panel), and to r_{-3}, where $X_{HI} = 10^{-3}$ (bottom panel). The shaded plots show the H II region sizes at 3.16×10^7 years (corresponding roughly to the Salpeter time, and to the expected ages of bright quasars; see, e.g., Martini 2004), as a function of the intrinsic absorption N_H and spectral index s.

Remember that the softest spectrum is in the lower right corner of the graph, while the hardest spectrum is in the upper left. The trend in both panels is for the radius to decrease with increasing N_H, as Q_{abs} decreases due to the absorption, and as more of the photons escape from the ionized region because of their longer MFP. Decreasing the spectral index s (which also produces a harder spectrum), on the other hand, results in a larger H II region, since the harder spectrum is less attenuated by the intrinsic absorption, meaning Q_{abs} is larger.

Considering both H II region size measurements together leads to an interesting conclusion. Several recent papers (Mesinger & Haiman 2004; Maselli et al. 2007; Lidz et al. 2007; Bolton & Haehnelt 2007a) have explored the accuracy of R_α and R_β, defined as the radii where the flux in the redshifted Lyα and Lyβ region of the spectrum falls below some fixed threshold, as a proxy for the location of the I–front. They found that R_α and R_β are biased measurements, underestimating the "true" distance to the I–front (which we might choose to locate at $r_{0.5}$) by typically 20–30%. Here we discover another effect to worry about: as the spectra get harder (and especially as the obscuring column increases), the radius of the highly ionized region r_{-3}, decreases much more quickly than the half-ionization radius $r_{0.5}$. This is because the harder photons are ineffective at
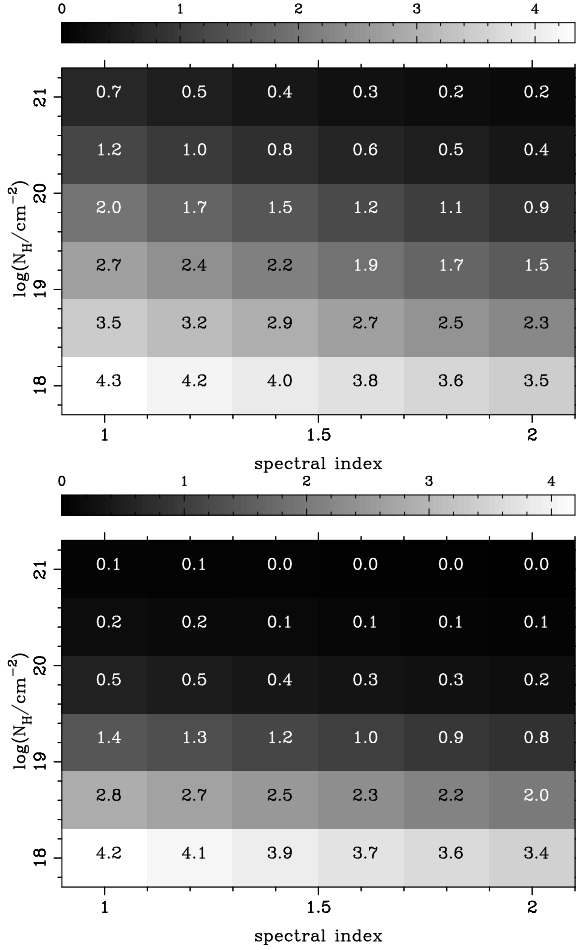
Figure 9. The size of the ionized region in Mpc out to $X_{HI} = 0.5$ ($r_{0.5}$, a) and $X_{HI} = 0.001$ (r_{-3}, b) versus the intrinsic absorption N_H (in cm^{-2}) and the spectral index s at 3.16×10^7 years and with $Q = 2 \times 10^{57}\,\mathrm{s}^{-1}$. Each block represents one simulation, with the size indicated in numerals and by the shading. The key to the shading appears at the top of each graph.

maintaining a high ionized fraction because of the low ionization cross section, instead tending to escape into more neutral gas farther out. This produces a thicker front and a more neutral H II region. For hard spectra, this significantly increases the bias, with the underestimate reaching values as high as a factor of ≈ 8 for the spectra with the largest obscuring column.

4 MEASURING THE THICKNESS OF THE I–FRONT

4.1 Front Thickness in 21cm and in Lyman Absorption Spectra

As mentioned above, we are interested in two different regions of the ionization front: the highly ionized inner face of the front at $10^{-3} \lesssim X_{HI} \lesssim 10^{-2.5}$ which is approximately the region probed by Lyman-series absorption spectra, and the less–ionized outer tail of the front at $0.1 \lesssim X_{HI} \lesssim 0.9$, which is the region potentially accessible to redshifted 21 cm observations.

Mesinger & Haiman (2004) proposed the idea that the difference between R_β and R_α, as defined in the previous section, could be useful to probe the spectral hardness, with the two values increasingly separated for harder spectra. In a subsequent study, Bolton & Haehnelt (2007a) simulated a large set of quasar Lyman α and β absorption spectra and studied the possibility of using the transmission window created by the ionized region around the quasar to constrain the mean ionization fraction of the IGM. They found that density fluctuations induce a large scatter in their measured quantity, which is the ratio of radii inferred from each spectrum R_β/R_α. However, according to their simulations, $R_\beta/R_\alpha = 1.2$ would be distinguishable from $R_\beta/R_\alpha = 1$ at the 2σ level with about 20 high-quality quasar spectra. As a proxy for this ratio, we use $r_{-2.5}/r_{-3}$, the ratio of radii at which $X_{HI} = 10^{-2.5}$ and $X_{HI} = 10^{-3}$, which correspond roughly to the points where flux would be lost in the Ly–β and Ly–α absorption spectra, respectively, for a typical deep Keck spectrum of a $z = 6$ quasar.

In contrast to the Lyman line absorption spectra, the 21cm observations will be sensitive, at $z = 6-10$, to features corresponding to neutral fractions of order unity, with regions that have $X_{HI} \lesssim 0.1$ corresponding to "holes" in tomographic 21cm maps. Although the effective spatial resolution of such maps is highly dependent on the specific interferometric instrument and its configuration, a rough target value for next–generation facilities may be ~ 1 physical Mpc (see, e.g., the review by Furlanetto et al. 2006). We adopt here $d_{0.1}$, the difference between the radius at which $X_{HII} = 0.1$ and $X_{HI} = 0.1$, as a proxy for the thickness of the I–front that may be measurable with 21 cm instruments.

Figure 10 depicts our measures of the ionization front thickness around a quasar with an age of $\sim 3.16 \times 10^7$ years, on the same grid of parameters used in Figure 9. The first panel shows $d_{0.1}$, which exceeds our estimated detection threshold of ~ 1 Mpc for a large region of the parameter space. The thickness increases with increasing spectral hardness up till $\log(N_H/\mathrm{cm}^{-2}) = 19.8$, after which is decreases as N_H increases, due to the overall shrinking of the ionized region discussed in § 3.3, and shown in Figure 9. This will be the pattern for most of the grids we will discuss: the $d_{0.1}$ widths will always increase with decreasing spectral index, and will grow with increasing absorption up to a point, but will eventually shrink for large enough N_H.

The $r_{-2.5}/r_{-3}$ ratio in the second panel is almost totally insensitive to the spectral index. Making the spectral index smaller does make the front slightly thicker, but it also moves the front outward by a small amount, which keeps the ratio constant. The ratio increases dramatically between $\log(N_H/\mathrm{cm}^{-2}) = 18.6$ and $\log(N_H/\mathrm{cm}^{-2}) = 19.2$, becoming large enough to be potentially detectable (according to the criterion defined above based on Bolton & Haehnelt 2007a), thanks to the fact that for the harder spectra r_{-3} reaches equilibrium faster, while $r_{-2.5}$ continues to move outward a little longer, which stretches out the ratio. The intrinsic absorption must be at least $\log(N_H/\mathrm{cm}^{-2}) = 19.2$ for the ratio to exceed 1.1. The ratio exceeds 1.2 for any spectral index at $\log(N_H/\mathrm{cm}^{-2}) \geq 19.8$.

Note that the contours for the two size measures in the N_H-s plane have different orientations. This is not surprising, since variations of s and N_H can affect the profile differently at different locations in the front. This suggests that a
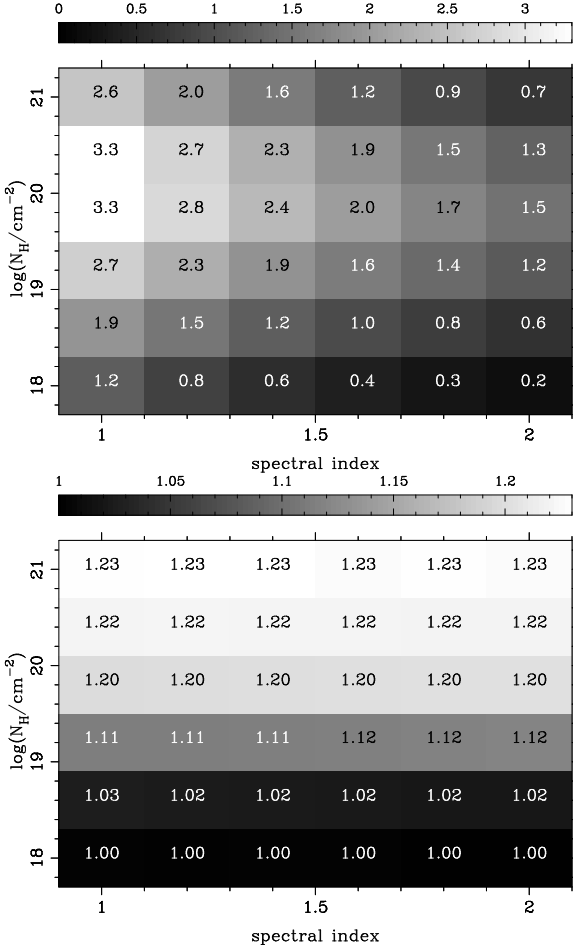
Figure 10 (top, $d_{0.1}$ in Mpc): colour scale 0 – 3

$\log(N_{\rm H}/{\rm cm}^{-2})$						
21	2.6	2.0	1.6	1.2	0.9	0.7
	3.3	2.7	2.3	1.9	1.5	1.3
20	3.3	2.8	2.4	2.0	1.7	1.5
	2.7	2.3	1.9	1.6	1.4	1.2
19	1.9	1.5	1.2	1.0	0.8	0.6
18	1.2	0.8	0.6	0.4	0.3	0.2

spectral index (1 – 1.5 – 2)

Figure 11 (top, $d_{0.1}$ in Mpc): colour scale 0 – 4

$\log(N_{\rm H}/{\rm cm}^{-2})$						
21	4.1	3.3	2.6	2.0	1.6	1.2
	5.0	4.1	3.4	2.8	2.3	1.9
20	4.7	4.0	3.4	2.8	2.4	2.1
	3.8	3.1	2.6	2.2	1.8	1.5
19	2.7	2.1	1.6	1.3	1.0	0.8
18	1.7	1.2	0.8	0.5	0.3	0.2

spectral index (1 – 1.5 – 2)

Figure 10 (bottom, $r_{-2.5}/r_{-3}$): colour scale 1 – 1.2

$\log(N_{\rm H}/{\rm cm}^{-2})$						
21	1.23	1.23	1.23	1.23	1.23	1.23
	1.22	1.22	1.22	1.22	1.22	1.22
20	1.20	1.20	1.20	1.20	1.20	1.20
	1.11	1.11	1.11	1.12	1.12	1.12
19	1.03	1.02	1.02	1.02	1.02	1.02
18	1.00	1.00	1.00	1.00	1.00	1.00

spectral index (1 – 1.5 – 2)

Figure 11 (bottom, $r_{-2.5}/r_{-3}$): colour scale 1 – 1.6

$\log(N_{\rm H}/{\rm cm}^{-2})$						
21	1.75	1.75	1.75	1.75	1.75	1.75
	1.74	1.74	1.74	1.74	1.74	1.74
20	1.72	1.72	1.72	1.72	1.73	1.73
	1.54	1.54	1.54	1.55	1.55	1.56
19	1.04	1.03	1.03	1.03	1.03	1.02
18	1.00	1.00	1.00	1.00	1.00	1.00

spectral index (1 – 1.5 – 2)

Figure 10. Ionization front thickness measures at 3.16×10^7 years as measured by $d_{0.1}$ (in Mpc, top) and $r_{-2.5}/r_{-3}$ (bottom).

Figure 11. Widths at 1×10^8 years as measured by $d_{0.1}$ (in Mpc, top) and $r_{-2.5}/r_{-3}$ (bottom).

combination of 21 cm and Lyman-series absorption measurements could break the degeneracy inherent in the separate observations and allow both parameters to be constrained simultaneously.

4.2 Parameter Variations

We next examine how our results change when we vary other model parameters.

4.2.1 Source Lifetime

In Figure 11, we show the same thickness measures as in Figure 10, but for quasar three times older, at $t = 10^8$ years. The figure reveals that the outer tail of the front ($d_{0.1}$) has generally gotten thicker, but otherwise follows the same trends we saw at 3.16×10^7 years. The inner face ratio $r_{-2.5}/r_{-3}$ has remained small and almost unchanged for the softest spectra with $N_{\rm H} \leq 10^{18.6} \, {\rm cm}^{-2}$. These spectra create steep fronts and deep equilibrium regions with $X_{\rm HI} < 0.001$, so even at 10^8 years $r_{-2.5}/r_{-3}$ is still measuring the steep slope of the rapid ionization zone. There is a sharp increase in the front thickness at all spectral indices between $N_{\rm H} = 10^{18.6}$ and $10^{19.2} \, {\rm cm}^{-2}$. This is because for the harder spectra the equilibrium region reaches $X_{\rm HI} > 10^{-3}$
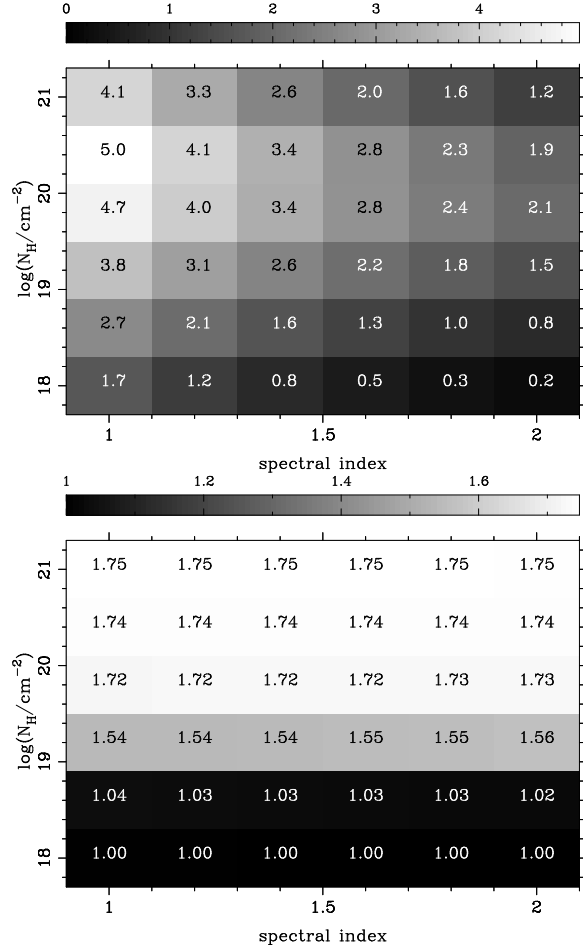
(but is usually still below $X_{\rm HI} = 10^{-2.5}$) before 10^8 years, meaning that r_{-3} is the distance to a fixed point in the equilibrium zone, while $r_{-2.5}$ is the distance to a point in the still-receding ionization front. This produces the high ratios seen in the figure.

4.2.2 Source Luminosity

Reducing the (pre-intrinsic-absorption) ionizing photon luminosity from $Q = 2 \times 10^{57} \, {\rm s}^{-1}$ to $2 \times 10^{56} \, {\rm s}^{-1}$ produces the widths shown in Figure 12. Reducing the luminosity by a factor of 10 reduces the time scale by a factor of 10 and the Strömgren radius by a factor of $10^{1/3} = 2.15$. The shape of the pre-ionization and rapid-ionization zones (since they are largely unaffected by recombinations) are therefore almost identical to the $Q = 2 \times 10^{57} \, {\rm s}^{-1}$ models at 3.16×10^6 years (not shown), when the same total number of photons has been emitted. And indeed the $d_{0.1}$ values are very close, and consequently are lower than the $Q = 2 \times 10^{57} \, {\rm s}^{-1}$ models at 3.16×10^7 years by a factor of about 1.5 to 2. The same reasoning does not apply to the $r_{-2.5}/r_{-3}$ ratio, which end up with similar values. The lower luminosity means that r_{-3} is frozen into the equilibrium zone earlier, but r_{-2} also moves out more slowly, so the ratio ends up similar to the higher luminosity case.
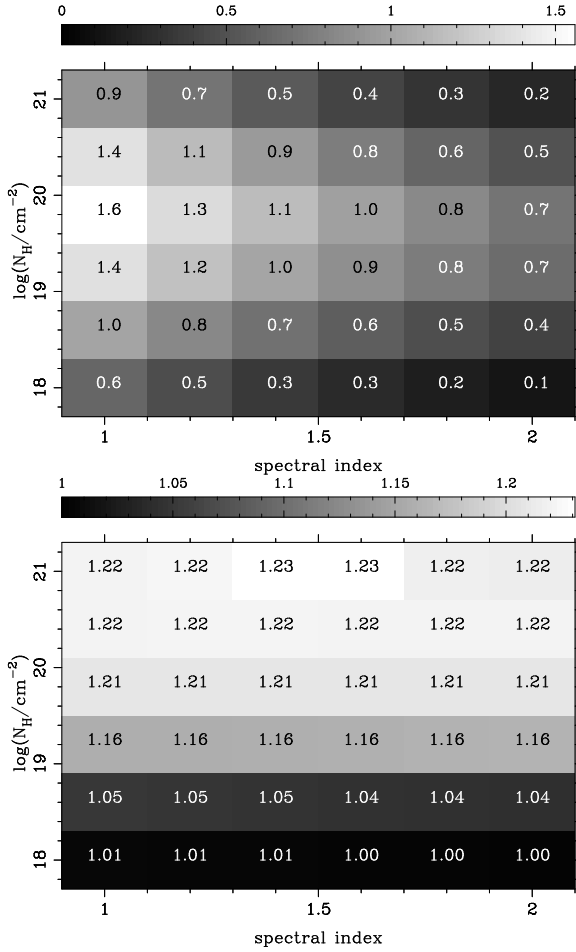
Figure 12. Widths with $Q = 2 \times 10^{56}$ s^{-1} at 3×10^7 years as measured by $d_{0.1}$ (in Mpc, top) and $r_{-2.5}/r_{-3}$ (bottom).

Figure 14. Widths with $C = 5$ at 3.16×10^7 years as measured by $d_{0.1}$ (in Mpc, top) and $r_{-2.5}/r_{-3}$ (bottom).
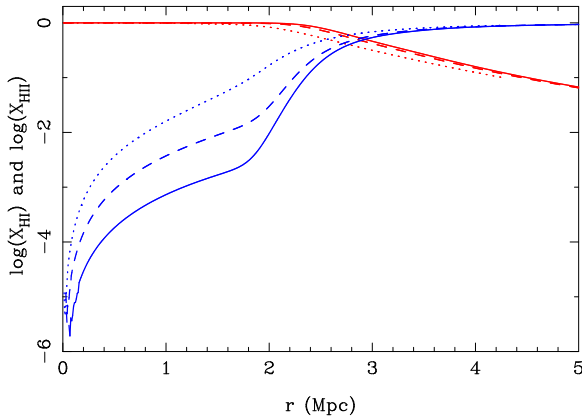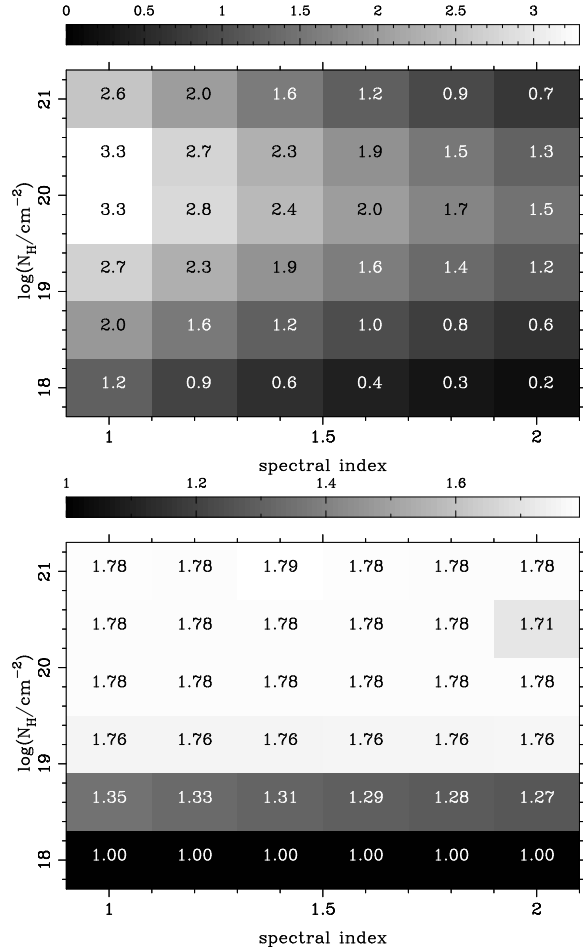

Figure 13. Ionized (red) and neutral (blue) hydrogen fractions for $C = 1, 5, 20$ (bottom-to-top for the neutral fraction) at $t = 10^8$ years. Spectral parameters are the same as in Figure 2.

ure 13. Increasing the clumping factor also decreases the recombination time and Strömgren radius. With $C = 5$, $t_{\rm rec} = 3.2 \times 10^8$ years, while with $C = 20$, $t_{\rm rec} = 8.1 \times 10^7$ years (both at $z = 6$), meaning that the ionization structure could approach equilibrium within a quasar lifetime.

Figure 14 reproduces the grids of spectral parameters with a clumping factor of $C = 5$. The thickness measures follow the same trends seen with $C = 1$. Increasing the clumping factor produces almost the same grid of $d_{0.1}$ values because it has little effect on the high-energy photons that pre-ionized the outer region.

The $r_{-2.5}/r_{-3}$ ratios on the $C = 5$ grid are quite a bit higher than with $C = 1$. The ratio exceeds 1.2 for all spectra with $N_{\rm H} \geq 10^{18.6}$ cm^{-2}. A clumping factor of $C = 20$ (also not shown) produces a very similar grid for the more obscured spectra, and produces even higher ratios for $\log(N_{\rm H}/{\rm cm}^{-2}) \leq 19.2$.

4.2.3 Clumping Factor

The clumping factor effectively increases the recombination coefficient, which has the effect of raising the neutral fraction in the equilibrium zone, but has little effect on the rapid-ionization or pre-ionization regions, (as emphasized in Cen & Haiman 2000), and as can be seen in Fig-

4.2.4 The Ionizing Background

The IGM is expected to have already undergone some non–negligible ionization by galaxies, and possibly by fainter quasars, by the time the massive black holes producing the observable $z \gtrsim 6$ quasars appear. The ionizing background may have both a smooth X-ray component (e.g.
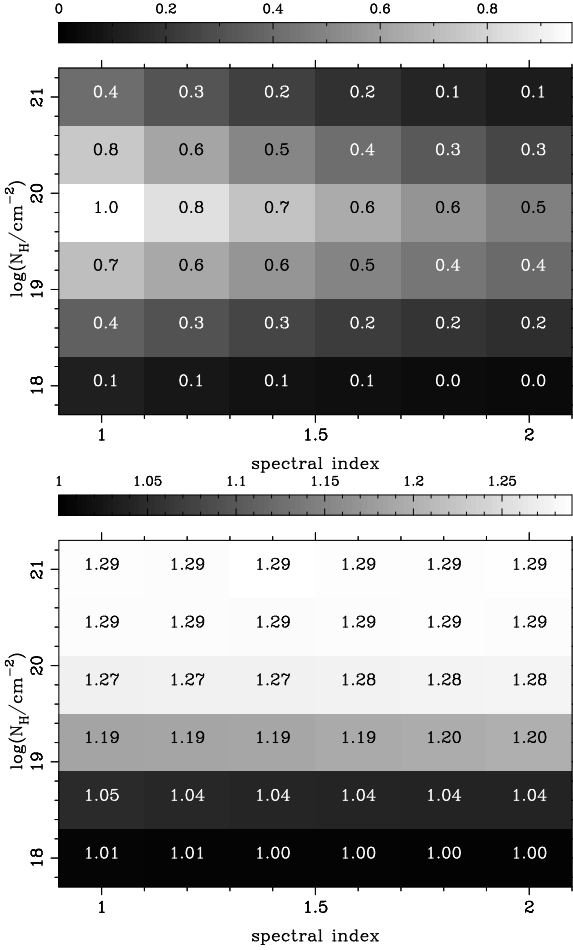
Figure 15. Widths with a uniform ionizing background, $X_{\mathrm{HII},BG} = 0.75$. Note the here we are using the distance from $X_{\mathrm{HII}} = 0.9$ to $X_{\mathrm{HII}} = 0.8$ to measure the outer front (top) and still using $r_{-2.5}/r_{-3}$ (bottom) for the inner front. Both are at 3.16×10^7 years.

Venkatesan et al. 2001; Oh 2001) from pre–existing fainter quasars, and a "swiss-cheese"-like component of smaller ionized bubbles surrounding (clusters of) galaxies, the latter of which may be highly clustered around the massive halos hosting our quasars of interest (e.g. Wyithe & Loeb 2007; Lidz et al. 2007; Alvarez & Abel 2007).

Here we first calculate a grid of thickness measures with a purely uniform background $\Gamma_{BG} = 4.4 \times 10^{-17}\,\mathrm{s}^{-1}$ (see the discussion of radiation transfer below), producing an equilibrium $X_{\mathrm{HII},BG} = 0.75$. We will then study three variations of this model, to address the following effects: (i) modification of the background flux due to radiative transfer effects caused by the ionization by the quasar, (ii) a non–uniform (swiss–cheese) background ionization topology, and (iii) enhanced ionization near the quasar due to clustering of pre–existing galaxies.

In the presence of a background, there are fewer neutral hydrogen atoms to ionize, and the ionization fronts travel farther in a given amount of time. The lower neutral hydrogen density also means the m.f.p. is longer, so the fronts are somewhat thicker. The equilibrium neutral fraction is relatively unaffected as long as it is well below $1 - X_{\mathrm{HII},BG}$. Setting $X_{\mathrm{HII},BG} = 0.75$ obviously makes our previously–

defined measure for the thickness, $d_{0.1}$, unusable, so we here instead examine the distance from $X_{\mathrm{HII}} = 0.9$ to $X_{\mathrm{HII}} = 0.8$ (and we can still use $r_{-2.5}/r_{-3}$). Both of these thickness–measures are shown in Figure 15, again at 3.16×10^7 years, as a function of spectral slope and obscuring column density.

The new measure of the outer part of the front behaves much like $d_{0.1}$ did for the grids with no background (except that it is obviously smaller overall). The figure also shows that $r_{-2.5}/r_{-3}$ is somewhat larger than for the no–background case. The reduced neutral hydrogen density allows the front to move more quickly, but has little affect on the equilibrium ionized fraction where $X_{\mathrm{HI}} \ll 1 - X_{\mathrm{HII},BG}$. This means that the inner (most highly ionized) edge of the front slows as it approaches the equilibrium value, while farther out the front is still receding at a faster rate, effectively thickening the front.

There is an inconsistency in the way the background ionization rate was added to the quasar flux above, however (which is shared by many other similar studies in the literature). We specified an ionization rate per neutral hydrogen atom Γ_{BG} which is constant, equivalent to a uniform background flux that does not depend on the ionization state of the gas. In fact, the flux from a homogeneous population of emitters will depend on the mean free path, and hence on the ionization state of the gas. The more highly ionized the gas is, the farther ionizing photons will travel through it, meaning that more distant sources can contribute to the local flux. In fact, the mean free path within a highly ionized H II region might exceed the size of the region, meaning that the background will be the sum of the flux from all the sources inside the region, and the background will grow as the region expands.

In a homogeneous medium with a total photon emission coefficient of j (photons per unit time per unit volume), the total incident flux (integrated over all angles) is simply[4]

$$J = \frac{j}{n_{\mathrm{H}}(1 - X_{\mathrm{HII}})\sigma} = j\,l_{\mathrm{MFP}} \qquad (14)$$

where σ is the absorption cross section for the photons. Since $\Gamma = J\sigma$, the background ionization rate should clearly depend on the ionization state of the gas. Similarly, the flux in the center of a sphere of radius r (where $l_{\mathrm{MFP}} \gg r$, and $j = 0$ outside the sphere) is $J = j\,r$.

In our model the medium is obviously not homogeneous, since X_{HII} varies with position and time (and later we will be interested in a variable j as well). Solving for the background flux J exactly in an inhomogeneous medium requires computationally expensive 3-D radiation transfer (and still 2-D in the azimuthally symmetric case), so we have implemented an approximate radiative transfer algorithm to estimate the effect using a 1-D calculation. We assume all of the background photons are at 13.6 eV and calculate the flux using the equation:

$$J(r) = J_0(r) + J_{\mathrm{in}}(r) + J_{\mathrm{out}}(r) \qquad (15)$$

$$J_0(r) \equiv j(r)\,l_{\mathrm{MFP}}(r)\,[1 - \exp(-\Delta r/l_{\mathrm{MFP}}(r))] \qquad (16)$$

---

[4] Usually an emission coefficient is defined as the amount of power emitted per unit solid angle per unit volume. Here we use a somewhat different definition which is convenient for the task at hand.
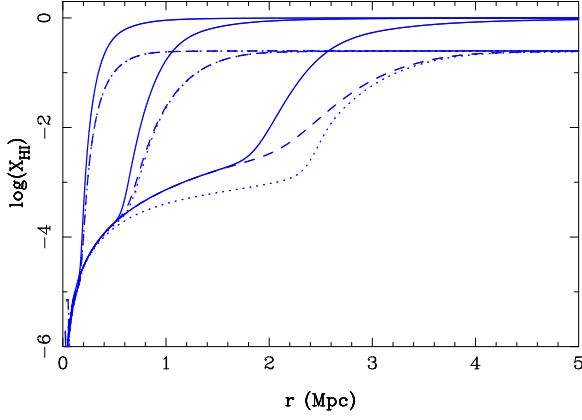
Figure 16. Comparison of neutral fraction with no ionizing background (solid), with a uniform background without background radiation transfer (dashed), and the same background with approximate RT (dotted) at $\log(t/\text{years}) = 6$, 7, and 8 (left to right). Spectral parameters are the fiducial ones used in Figure 2 and the backgrounds are chosen to produce $X_{\text{HII},BG} = 0.75$. Note that the RT effects make a noticeable difference in the 10^8 year case: the reduction of the mean free path by the quasar boosts the contribution of background galaxies to the total ionization rate inside the H II region.

$$J_{\text{in}}(r) \equiv \frac{1}{2} \int_0^{r-\Delta r} j(r') \left(\frac{r'}{r}\right)^2 e^{[\tau_0(r')-\tau_0(r)]} dr' \qquad (17)$$

$$J_{\text{out}}(r) \equiv \frac{1}{2} \int_{r+\Delta r}^{\infty} j(r') e^{[\tau_0(r)-\tau_0(r')]} dr' \qquad (18)$$

where the first term is the flux from within one radial step Δr, the second term is the estimated flux from within $r - \Delta r$, the third term is the estimate flux from outside of $r + \Delta r$, and $\tau_0(r)$ is the optical depth at 13.6 eV as defined by equation 1. The *ad hoc* factor $\left(\frac{r'}{r}\right)^2$ is used to decrease the contribution to the flux from spherical shells at small r (roughly approximating the decrease in the total emitting volume in 3D at small radii). At $r \gg l_{\text{MFP}}$ with uniform j and X_{HII}, equation 15 reproduces the analytical result (equation 14).

Figure 16 compares the ionization structures with and without the approximate RT algorithm. The photon emission coefficient is $j = \alpha_B n_{\text{H}}^2 X_{\text{HII},BG}^2 = 8.3 \times 10^{-22}\,\text{s}^{-1}\text{cm}^{-3}$. For quasar ages of $\lesssim 10^7$ years, the radiation transfer makes no difference to the ionization structure. The central ionized region is simply too small to allow a large additional background to build up. At 10^8 years, RT decreases the neutral fraction, but only for $-4 \lesssim \log(X_{\text{HI}}) \lesssim -1.5$. This is because the ionized region has grown large enough for the diffuse background to become significant, but the quasar flux still dominate close the quasar, and the MFP is still very small for 13.6 eV photons once the neutral fraction gets large, so the extra flux is confined to the inner part of the front. We conclude that radiation transfer of flux from a uniform ionizing background could be important for Lyman-series observations of old quasars or with high backgrounds, but will be less important for 21 cm observations.

Next, let us examine the effect of a patchwork of pre-existing ionized bubbles along our line of sight. This is the type of background profile that results from the "swiss-cheese" topology of small ionized bubbles (generated by
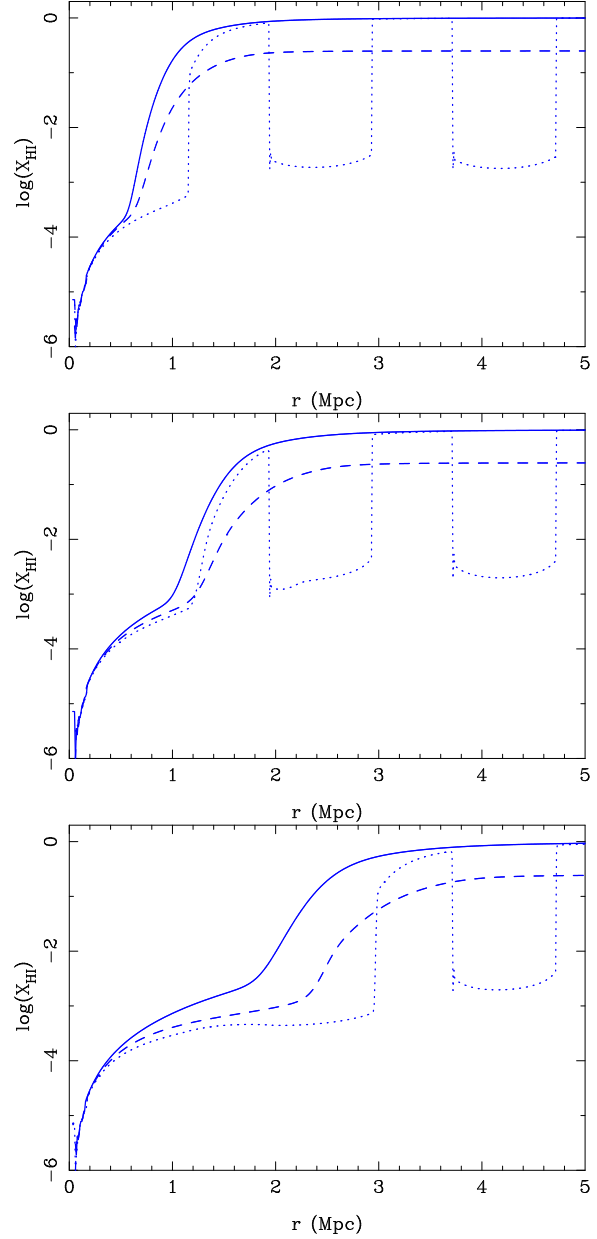

Figure 17. Comparison of the neutral fraction with no ionizing background (solid), with a smooth ionizing background (and approximate radiation transfer) chosen to produce $X_{\text{HII},BG} = 0.75$ (dashed) and with a "swiss-cheese" background (dotted) of 1 Mpc ionized bubbles separated by 0.79 Mpc neutral regions, which would produce a similar average ionization. Spectral parameters are the fiducial ones used in Figure 2. The panels show the ionization structures at 10^7, 3×10^7, and 10^8 years, respectively.

neighboring galaxies and possibly AGN) embedded in a neutral IGM. Naively, we might choose to fill 75% of the IGM with ionized bubbles in order to compare this scenario with the smooth background of Figure 16, but here we have to be careful about what quantities we want to compare. The recombination rate in a fully ionized region is $\alpha_B n_{\text{H}}^2 = 1.48 \times 10^{-21}\,\text{s}^{-1}\text{cm}^{-3}$, so if a fraction f_{ion} of the universe is contained in ionized bubbles, then the average photon emission coefficient needed to maintain equilibrium is $j = \alpha_B n_{\text{H}}^2 f_{\text{ion}}$. Equating this to the coefficient for the

smooth $X_{\mathrm{HII},BG} = 0.75$ case we obtain $f_{\mathrm{ion}} = 0.75^2 = 0.56$. In fact we will need an even higher background in the bubbles in order for them to be highly ionized, as we will discuss below.

Next we need to determine the size of the ionized bubbles. Furlanetto et al. (2004) calculated that when 56% of the IGM was contained in galactic H II regions, the H II region radius distribution peaked at ~ 4 Mpc comoving, or about 0.6 physical Mpc at $z = 6$. We have set up a background ionization profile consisting of evenly-spaced ionized regions with a diameter of 1 Mpc, occupying 56% of the IGM volume (and therefore separated by neutral regions of 0.79 Mpc along the LOS). The neutral fraction within the bubbles is initially set to 10^{-3}. The background needed to maintain this level of ionization is

$$j = \frac{\alpha_B \, n_{\mathrm{H}} \, X_{\mathrm{HII},BG}^2}{\sigma_0 \, r \, (1 - X_{\mathrm{HII},BG})} = 2.01 \times 10^{-21} \, \mathrm{s}^{-1}\mathrm{cm}^{-3} \qquad (19)$$

where $r = 0.5$ Mpc is the radius of the bubble. This is 35% higher than the background in the smooth case. We again use equation 15 to approximate radiation transfer for the background photons.

The resulting ionization structure is shown in Figure 17. Without the background, the fronts in the inter-bubble regions would be essentially the same shape as they are in totally neutral IGM, except sliced and shifted apart where the bubbles occur, since the ionizing radiation traverses the bubbles unabsorbed (except by helium and the small amounts of residual hydrogen) so the front can pick up where it left off on the other side. The presence of helium and the geometric dilution cause some changes in the shape, but the background radiation transfer has a greater effect. Once the front has swept past a bubble, it's background photons can escape, and they stream out to contribute to the ionization of the inter-bubble regions.

This type of background structure may have interesting observational manifestations. Within the inter-bubble regions, the front is somewhat thinner than with either no background or a smooth background. The front is thinner than in the no-background case because the background photons contributing to the movement of the front have a short MFP. The front is thinner than in the smooth-background case because it is "trapped" by the fully neutral inter-bubble regions where the mean free path is short, so it is slowed down, meaning that a more highly ionized part of the front (e.g. r_{-3}) can "keep up" better with a more neutral part (e.g. $r_{-2.5}$), resulting in a thinner front over all. There will be brief windows when r_{-3} is still trapped in the residual neutral gas on one side of a bubble, while $r_{-2.5}$ is on the far side, but it would require detailed simulations of absorption spectra to determine the observability of such a situation. The shape of the front at neutral fractions more relevant to 21 cm observations again tends to suggest smaller thickness measurements, but it seems likely that the thicknesses could still be measurable.

The signature of the hard quasar spectrum is also still quite visible on large scales, for instance in the separation between $X_{\mathrm{HI}} \sim 10^{-4}$ and $X_{\mathrm{HI}} \sim 0.1$. This suggests that a combination of 21 cm and Lyman-series observations, particularly when smoothed on large scales or averaged over many quasars, could place constraints on the ionizing SED of the quasar or quasars. If the patchy ionization structure is
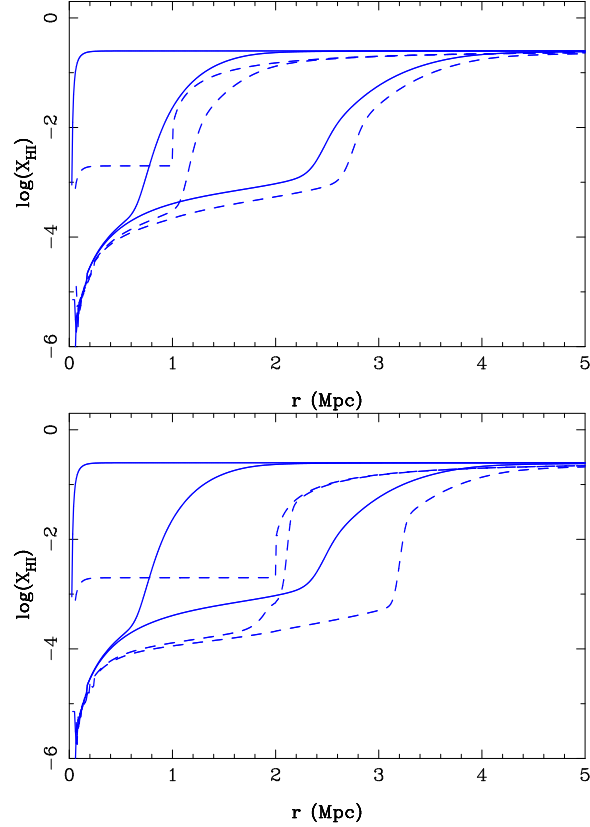

Figure 18. Comparison of the neutral fraction with a uniform ionizing background (solid) and a biased background from pre–existing galaxies clustered around the quasar (dashed). Approximate background RT is used in both cases. Spectral parameters are the fiducial ones used in Figure 2. The three sets of curves correspond to source ages of $\log(t/\mathrm{years}) = 4$, 7 and 8, respectively. In the first panel, the central pre-ionized bubble has a radius of 1 Mpc, while in the second panel the radius is 2 Mpc.

resolved in future, high–resolution 21cm observations with SKA, then the thickness of the front in–between the individual galaxy–bubbles can reveal evidence for a hard quasar spectrum separately along each direction measured from the quasar.

Finally, we consider the effect of clustering of background sources around the quasar. Wyithe & Loeb (2007) have explored the mean ionization structure around a quasar resulting from the biased clustering of galaxies around its host halo (not addressing the discreteness of the bubbles in the radial profile). They point out that even outside the I-front, the IGM is ionized 10-20% more than the global mean ionized fraction. While a high–resolution 21cm interferometer, such as SKA, could resolve such clusters of galaxy–bubbles outside the quasar's H II region, the next generation of experiments will likely not have sufficient resolution. In this case, the I–front will appear extended due to the presence of galaxies.

In order to explore the effect of such a pre–ionization profile on our conclusions, we implemented an ionizing background designed to qualitatively mimic the background ionization structure predicted by Wyithe & Loeb (2007) when the IGM far from the quasar is at $X_{\mathrm{HII},BG} \sim 0.7$–0.8. In this scenario pre–existing galaxies produce an H II region

centered on the quasar; outside this H II region, there is a tail of excess partial ionization, slowly approaching the background level of the neutral fraction in the IGM.

To produce the first panel in Figure 18, we set up an ionizing background to produce a 1 Mpc radius inner ionized region (initially set at $X_{\rm HII} = 2 \times 10^{-3}$ with $j = 4.41 \times 10^{-21}$ s^{-1}cm^{-3}). Outside of that, the profile is set to

$$X_{\rm HII,BG} = 0.75 + \left[\frac{(r/{\rm Mpc}) + 1.91}{1.81} \right]^{-3}, \qquad (20)$$

with $j = \alpha_B \, n_{\rm H}^2 \, X_{\rm HII,BG}^2$ for $r > 1$ Mpc. In the second panel the radius of the pre-ionized region is increased to 2 Mpc and the outer profile is shifted accordingly.

Figure 18 illustrates what happens to the I–front as it passes through such a biased background. The dashed curves show the I–front expanding into the pre–ionized region, contrasted with the case when the pre–ionization is uniform (solid curves). The figure reveals that once the front has passed beyond the high-background inner region, it quickly begins to approach the shape of the ionization profile in a uniform background, though the extra flux from the sources clustered close to the quasar keeps it ahead of the front in the uniform case. The presence of helium is particularly important in this case because it determines the speed at which the front can propagate through the pre-ionized region (since helium is assumed to be unaffected by the background and therefore still neutral). We have actually chosen rather small sizes for our central pre-ionized region. Wyithe & Loeb (2007) predict central regions of $r \sim 2$–8 Mpc when $X_{\rm HII,BG} \sim 0.7$–0.8. A larger region implies a larger background flux once the front has passed the inner region. This would prolong the time during which the front shape is affected by the background bias. Even a region as small as 2 Mpc results in fronts whose inner parts are significantly less broad at 10^8 years, as seen in the second panel.

5 CAVEATS

Before we summarize our conclusions, let us briefly review the limitations of the methods we have employed in reaching them.

The one-the-spot approximation — in which we assume that ionizing photons produced by recombination are absorbed at their point of origin — is strictly valid only where the mean free path of the recombination photons is much shorter than other length scales of interest, such as the thickness of the front.[5] This condition is violated where the neutral fraction is very low, in the inner part of the ionized region. It is also less accurate for helium-derived photons, since they are generally more energetic. The result is a slight overestimate of the ionization rates, and therefore a slight underestimate of the neutral fraction, close to the quasar. The effect is less important for harder spectra (because they leave higher neutral fractions overall), and is unimportant

---

[5] The situation is slightly different for soft (e.g. stellar) spectra, in which the mean ionizing photon from the source is also close to the threshold. In that case both the source spectrum and the recombination radiation are concentrated near the threshold. See Osterbrock & Ferland (2006).

in the outer part of the front. For instance, the mean free path at 13.6 eV, $l_{\rm MFP}(\nu_0) < 0.01$ Mpc for $X_{\rm HI} > 0.07$.

We have ignored the propagation time for photons (due to the finite speed of light). Our results accurately predict the observed structure along a line of sight aimed directly at the quasar, in an absorption spectrum, for example. To simulate two dimensional projections of the ionization structure (like 21 cm maps), we would need to apply a simple transformation (see citations in § 2.1). In fact, since the thickness of the I–front varies with time, in principle, a comparison of the thickness in transverse and radial directions, in addition to the angular dependence of the overall bubble size due to finite–speed–of light effects (Wyithe et al. 2005; Yu 2005; Shapiro et al. 2006), will contain information about the age of the quasar.

We have assumed the density of the IGM surrounding the quasar is homogeneous on a macroscopic scale, with smaller variations accounted from by a uniform clumping factor. Quasars are actually expected to form in biased environmental conditions, with high gas density and a high density of neighboring halos. The largest effect would be along lines of sight that intersect high-density Lyman limit systems, which could stall the propagation of the I–front and shield the gas further along the LOS from ionizing photons. The less extreme effects of density inhomogeneities would be somewhat ameliorated by certain observational necessities. In order to get a large enough signal to noise ratio to meaningfully constrain the structure of quasar H II regions, it may be necessary to stack 21 cm images of multiple bubbles. Similarly, measurements of the spectra of many quasars would be combined in order to constrain the ionization structure with Lyman-series absorption observations. In either case, density inhomogeneities would add to the random "noise", but could, to some extent, be averaged out. Width measurements may be more robust under such conditions than the simple size measurements discussed by Maselli et al. (2007), however more study is needed to determine that conclusively.

As mentioned in section 2.4, we have assumed the IGM is isothermal, justifying this by pointing out that most of the heating will occur before recombinations become important. Therefore, as long as we choose the gas temperature to match conditions expected inside the H II region, this assumption should have little effect on our results.

Finally, we should remind the reader that since we did not actually simulate absorption spectra, we have not taken into account the effect of the GP trough damping wing (from the neutral hydrogen surrounding the ionized region), which could be very important for the observational determination of R_β/R_α. In fact, Mesinger & Haiman (2004) essentially use this effect to constrain the neutral hydrogen fraction in the IGM.

6 DISCUSSION AND CONCLUSIONS

We have found that high-redshift quasars residing in a partially neutral IGM could produce ionization fronts with an observable thickness, given a sufficiently hard ionizing spectrum. We discovered that simulating the time-dependent evolution of the front is crucial for making accurate predictions of the ionization structure, and that the presence

of helium in the IGM and secondary ionizations by high-energy photoelectrons can both have significant effects on the ionization structure.

With an intrinsic hydrogen column density $\log(N_{\rm H}/{\rm cm}^{-2}) \gtrsim 19.2$ or a sufficiently hard power–law spectrum combined with some obscuration (e.g. spectral index $s \lesssim 1.2$ at $\log(N_{\rm H}/{\rm cm}^{-2}) \gtrsim 18.0$), the outer thickness of the front exceeds ~ 1 physical Mpc and may be measurable from the three–dimensional morphology of its redshifted 21cm signal.

The highly ionized inner part of the front, which may be probed by Lyman line absorption spectra, remains thin for bright quasars unless a large obscuring column ($\log(N_{\rm H}/{\rm cm}^{-2}) \gtrsim 19.2$) removes most of their ionizing photons up to ≈ 40 eV. Otherwise the lowest energy photons with the shortest mean free paths always dominate ionization at the inner face of the front resulting in a small thickness.

Highly absorbed ionizing spectra leave a relatively large neutral fraction within the H II region, which means that the Lyman-series optical depths can be large even within the front. For sources with $\log(N_{\rm H}/{\rm cm}^{-2}) \gtrsim 19.8$, the Lyman α trough (where the neutral fraction is $\gtrsim 10^{-3}$) underestimates the size of the H II region by a factor of $\gtrsim 4$. The bias can get as large as a factor of ≈ 8 within out parameter space. This is in addition to other effects that bias this measurement by a much smaller amount, as already discussed by several authors (Maselli et al. 2007; Lidz et al. 2007; Bolton & Haehnelt 2007a).

These obscured spectra also result in a large difference between the sizes measured by the Lyman α trough, and those measured by the Lyman β trough (where the neutral fraction is $\gtrsim 10^{-2.5}$). We estimate that R_β/R_α could be higher than 1.2 for $\log(N_{\rm H}/{\rm cm}^{-2}) \gtrsim 19.8$ with a quasar age of 3×10^7 years.

We explored the effects of uniform and non-uniform ionizing backgrounds, finding that even with a large uniform background the thickness of the ionization front has the potential to constrain the spectral parameters of the quasar. An ionization front propagating into a "swiss-cheese" background of small pre-ionized bubbles obviously makes for a more complicated ionization structure, but again, the shape of the front on both large and small scales is controlled largely by the quasar's ionizing SED. The greatest challenge is presented by a quasar turning on within a large pre-existing ionized region due to galaxies clustered around the quasar. In this case, the thickness of the front does not reflect the quasar's spectrum until the quasar has pushed the front a significant distance farther into the IGM. A measurement of a thin front around a quasar cannot, therefore, be interpreted as definitive evidence of a soft or unabsorbed quasar spectrum. On the other hand, measuring a thick front does suggest a highly absorbed quasar spectrum, because the galactic sources producing the pre-quasar ionization should be soft.

Shapiro et al. (2004) and Thomas & Zaroubi (2007) have also used 1-D radiative transfer calculations (with slightly different numerical methods) to explore high-redshift ionization structures, with the addition of self-consistent temperature calculations. Thomas & Zaroubi (2007) also included collisional ionization, and an evolving

mean IGM density, while Shapiro et al. (2004) (who were focused on the evaporation of minihalos by the I-front) included gas dynamics and trace metals. Like the present work, Thomas & Zaroubi (2007) included secondary ionizations, and both papers included helium, and calculations of the time evolution of the front. Neither paper included the ionization of hydrogen by helium recombination radiation, and they explored only blackbody (stellar) and power-law or truncated power-law (quasar or "miniquasar") sources, rather that the ultra luminous obscured quasars that we are interested in here (though the miniquasar spectra are fairly similar to some of our spectra). Shapiro et al. (2004) found, as we did here, that I–fronts around sources with harder spectra are thicker. However, they studied sources at higher redshift ($z = 9$), which were much less luminous, and the hardest spectrum they examined (a 10^5 K blackbody, representing pop III stars) was still softer than most of the spectra in the range included in the present paper. As a result, they found fronts much thinner (up to ~ 0.01 Mpc; see their Figures 7 and 8) than most of those discussed in the present paper. Among the many interesting findings of Thomas & Zaroubi (2007) are several relevant to the present study. Even with their harder power-law spectrum ($s = 1$ extending from 200–10^4 eV), they did not find extended ionization tails outside of the front, due to the combination of shorter lifetimes and higher redshift (when the IGM density was higher). They do, however, find an extended kinetic temperature structure coupled to the spin temperature so as to be observable with 21 cm instruments, and find that such observations could be useful in discriminating between various source spectra.

Finally, we found that the contours of degeneracy in our parameter space for measurements using 21 cm observations are oriented differently from those for measurements using Lyman-series absorption spectra. This suggests that studies combining both types of observations have the potential to break the degeneracy and constrain both the intrinsic absorption column and spectral index of a quasar's ionizing radiation at $z > 6$.

7   ACKNOWLEDGMENTS

REFERENCES

Alvarez M. A., Abel T., 2007, MNRAS, 380, L30
Bolton J. S., Haehnelt M. G., 2007a, MNRAS, pp L81+
Bolton J. S., Haehnelt M. G., 2007b, MNRAS, 374, 493
Cantalupo S., Porciani C., Lilly S. J., 2007, ApJ, in press, preprint arXiv:0709.0654"
Cen R., Haiman Z., 2000, ApJL, 542, L75
Dijkstra M., Haiman Z., Loeb A., 2004, ApJ, 613, 646

Dijkstra M., Wyithe J. S. B., Haiman Z., 2007, MNRAS, 379, 253

Fan X., Narayanan V. K., Strauss M. A., White R. L., Becker R. H., Pentericci L., Rix H.-W., 2002, AJ, 123, 1247

Ferguson J. W., Ferland G. J., 1997, ApJ, 479, 363

Flower D. R., Perinotto M., 1980, MNRAS, 191, 301

Furlanetto S. R., Oh S. P., Briggs F. H., 2006, Phys. Rep., 433, 181

Furlanetto S. R., Zaldarriaga M., Hernquist L., 2004, ApJ, 613, 1

Hui L., Gnedin N. Y., 1997, MNRAS, 292, 27

Hummer D. G., Seaton M. J., 1964, MNRAS, 127, 217

Hummer D. G., Storey P. J., 1998, MNRAS, 297, 1073

Iliev I. T., Ciardi B., Alvarez M. A., Maselli A., Ferrara A., Gnedin N. Y., Mellema G., Nakamoto T., Norman M. L., Razoumov A. O., Rijkhorst E.-J., Ritzerveld J., Shapiro P. R., Susa H., Umemura M., Whalen D. J., 2006, MNRAS, 371, 1057

Just D. W., Brandt W. N., Shemmer O., Steffen A. T., Schneider D. P., Chartas G., Garmire G. P., 2007, ApJ, 665, 1004

Lidz A., McQuinn M., Zaldarriaga M., 2007, ApJ, submitted, preprint arXiv:astro-ph/0703667

Madau P., Rees M. J., 2000, ApJL, 542, L69

Martini P., 2004, in Ho L. C., ed., Coevolution of Black Holes and Galaxies QSO Lifetimes. pp 169–+

Maselli A., Gallerani S., Ferrara A., Choudhury T. R., 2007, MNRAS, 376, L34

Mesinger A., Haiman Z., 2004, ApJL, 611, L69

Mesinger A., Haiman Z., 2007, ApJ, 660, 923

Oh S. P., 2001, ApJ, 553, 499

Osterbrock D. E., Ferland G. J., 2006, Astrophysics of Gaseous Nebulae and Active Galatic Nuclei, second edn. University Science Books, Sausalito, California

Ota K., Iye M., Kashikawa N., Shimasaku K., Kobayashi M. A. R., Totani T., Nagashima M., Morokuma T., Furusawa H., Hattori T., Matsuda Y., Hashimoto T., Ouchi M., 2007, ApJ, submitted, preprint arXiv:0707.1561

Porquet D., Reeves J. N., O'Brien P., Brinkmann W., 2004, A&A, 422, 85

Sazonov S. Y., Ostriker J. P., Sunyaev R. A., 2004, MNRAS, 347, 144

Shapiro P. R., Giroux M. L., 1987, ApJL, 321, L107

Shapiro P. R., Iliev I. T., Alvarez M. A., Scannapieco E., 2006, ApJ, 648, 922

Shapiro P. R., Iliev I. T., Raga A. C., 2004, MNRAS, 348, 753

Shemmer O., Brandt W. N., Schneider D. P., Fan X., Strauss M. A., Diamond-Stanic A. M., Richards G. T., Anderson S. F., Gunn J. E., Brinkmann J., 2006, ApJ, 644, 86

Shull J. M., van Steenberg M. E., 1985, ApJ, 298, 268

Songaila A., Cowie L. L., 2002, AJ, 123, 2183

Telfer R. C., Zheng W., Kriss G. A., Davidsen A. F., 2002, ApJ, 565, 773

Thomas R. M., Zaroubi S., 2007, MNRAS, in press, preprint arXiv:0709.1657"

Venkatesan A., Giroux M. L., Shull J. M., 2001, ApJ, 563, 1

White R. L., Becker R. H., Fan X., Strauss M. A., 2003, AJ, 126, 1

Wyithe J. S. B., Loeb A., 2004, Nature, 427, 815

Wyithe J. S. B., Loeb A., 2007, MNRAS, 374, 960

Wyithe J. S. B., Loeb A., Barnes D. G., 2005, ApJ, 634, 715

Yan M., Sadeghpour H. R., Dalgarno A., 1998, ApJ, 496, 1044

Yu Q., 2005, ApJ, 623, 683

Yu Q., Lu Y., 2005, ApJ, 620, 31

Zaroubi S., Silk J., 2005, MNRAS, 360, L64